Nanostructured N/S doped carbon dots/mesoporous silica nanoparticles and PVA composite hydrogel fabrication for anti-microbial and anti-biofilm application

Pisut Pongchaikul [a,1], Tasnim Hajidariyor [b,1], Navarat Khetlai [b,1], Yu-Sheng Yu [c], Pariyapat Arjfuk [a], Pongtanawat Khemthong [d], Wanwitoo Wanmolee [d], Pattaraporn Posoknistakul [b], Navadol Laosiripojana [e], Kevin C.-W. Wu [c,f,g,h,*], Chularat Sakdaronnarong [b,**]

[a] *Chakri Naruebodindra Medical Institute, Faculty of Medicine Ramathibodi Hospital, Mahidol University, Samut Prakarn 10540, Thailand*
[b] *Department of Chemical Engineering, Faculty of Engineering, Mahidol University, 25/25 Putthamonthon 4 Road, Salaya, Putthamonthon, Nakhon Pathom 73170, Thailand*
[c] *Department of Chemical Engineering, National Taiwan University, No.1, Sec.4 Roosevelt Road, Taipei 10617, Taiwan*
[d] *National Nanotechnology Center (NANOTEC), National Science and Technology Development Agency (NSTDA), Pathum Thani 12120, Thailand*
[e] *The Joint Graduate School of Energy and Environment, King Mongkut's University of Technology Thonburi, 126 Pracha Uthit Road, Bang Mot, Thung Khru, Bangkok 10140, Thailand*
[f] *Department of Chemical Engineering and Materials Science, Yuan Ze University, Chung-Li, Taoyuan, Taiwan*
[g] *International Graduate Program of Molecular Science and Technology, National Taiwan University (NTU-MST), Taipei 10617, Taiwan*
[h] *National Health Research Institute, Zhunan: 35, Keyan Road, Zhunan Town, Miaoli County 350, Taiwan*

ARTICLE INFO

ABSTRACT

Regarding the convergence of the worldwide epidemic, the appearance of bacterial infection has occasioned in a melodramatic upsurge in bacterial pathogens with confrontation against one or numerous antibiotics. The implementation of engineered nanostructured particles as a delivery vehicle for antimicrobial agent is one promising approach that could theoretically battle the setbacks mentioned. Among all nanoparticles, silica nanoparticles have been found to provide functional features that are advantageous for combatting bacterial contagion. Apart from that, carbon dots, a zero-dimension nanomaterial, have recently exhibited their photoresponsive property to generate reactive oxygen species facilitating to enhance microorganism suppression and inactivation ability. In this study, potentials of core/shell mesoporous silica nanostructures (MSN) in conjugation with carbon dots (CDs) toward antimicrobial activity against *Staphylococcus aureus, Pseudomonas aeruginosa* and *Escherichia coli* have been investigated. Nitrogen and sulfur doped CDs (NS/CDs) conjugated with MSN which were cost effective nanoparticles exhibited much superior antimicrobial activity for 4 times as much as silver nanoparticles against all bacteria tested. Among all nanoparticles tested, 0.40 M NS/CDs@MSN showed the greatest minimal biofilm inhibitory at very low concentration (< 0.125 mg mL^{-1}), followed by 0.20 M NS/CDs@MSN (0.5 mg mL^{-1}), CD@MSN (25 mg mL^{-1}), and MSN (50 mg mL^{-1}), respectively. Immobilization of NS/CDs@MSN in polyvinyl alcohol (PVA) hydrogel was performed and its effect on antimicrobial activity, biofilm controlling efficiency, and cytotoxicity toward fibroblast (NIH/3 T3 and L-929) cells was additionally studied for further biomedical applications. The results demonstrated that 0.40 M NS/CDs-MSN@PVA hydrogel exhibited the highest inhibitory effect on *S. aureus* > *P. aeruginosa* > *E. coli*. In addition, MTT assay revealed some degree of toxicity of 0.40 M NS/CDs-MSN@PVA hydrogel against L-929 cells by a slight reduction of cell viability from 100% to 81.6% when incubated in the extract from 0.40 M NS/CDs-MSN@PVA hydrogel, while no toxicity of the same hydrogel extract was detected toward NIH/3 T3 cells.

1. Introduction

Owing to the rising of a global epidemic, the upsurge of antimicrobial resistance has led to a crucial increase in bacterial pathogens that are resistant to one or multiple antibiotics (Dabke and Sheridan, 2011; Ferri et al., 2017; Merlino, 2017). Antibiotic confrontation is strongly connected to the formation of bacterial biofilms. This is due to the fact that the bacterial cells residing within the biofilm, protected by their self-produced biomatrix, demand a much higher concentration of antimicrobial agents compared to what is sufficient to eliminate their free-floating counterparts (planktonic bacteria). In some cases, this required concentration can be up to 1000 times greater, posing significant obstacles in devising effective treatment strategies for eradicating bacterial infections (Bjarnsholt, 2013).

In this context, nanomedicine has brought about promising advancements in clinical practice, enabling researchers to tackle previously unmet medical needs. Notably, nanoparticles serve as carriers for antibiotics, enhancing their ability to penetrate bacterial biofilms that have developed resistance to conventional antibiotics (Mishra et al., 2023). Within the extensive spectrum of nanoparticles, silica nanoparticles (SiNPs) stand out as a distinct class of inorganic nanoparticles possessing a diverse range of functional properties that offer competitiveness in opposing against bacterial infections (Martínez-Carmona et al., 2018; Şen Karaman et al., 2018). Particularly, mesoporous silica nanoparticles (MSNs) have garnered significant attention in nanomedicine. This is due to their favorable characteristics, such as good biocompatibility, high porosity, extensive surface area, substantial pore volume, and the ease of their surface modification to accommodate organic and inorganic therapeutic agents targeting bacterial infections (Bernardos et al., 2019; Castillo and Vallet-Regí, 2021; Manzano and Vallet-Regí, 2018; Selvarajan et al., 2020). Consequently, this study utilized functionalized and fully characterized MSNs as therapeutic agents to prevent the development of bacterial infections and study on their antibiofilm formation.

It has been widely known that metal/silica nanoparticle composite or metallodrugs exhibited excellent stimuli-response effect toward either controlled release of therapeutic agents or reactive oxygen species (ROS) generation to inactivate microorganisms. Copper (Díaz-García et al., 2020; Díaz-García et al., 2019), silver (Abbasi et al., 2023; Wang et al., 2014), platinum (del Hierro et al., 2017; Wani et al., 2016), tin (Bulatović et al., 2014), and titanium (del Hierro et al., 2017) were commonly used in this sense. Previous research revealed that silica mesoporous nanoparticles were modified with three different types of fluoroquinolones, and further loaded with Cu^{2+} or Ag^+ species. The Cu^{2+}-loaded materials displayed antibacterial effects against *Staphylococcus aureus* and *Escherichia coli*, possibly attributed to the higher generation of reactive oxygen species (ROS) which was observed to increase up to three times. On the other hand, the Ag^+-loaded materials exhibited a broader range of antibacterial activity, including inhibition against clinical strains of multi-drug-resistant *S. aureus* and *Pseudomonas aeruginosa* (Ugalde-Arbizu et al., 2023).

Carbon dots (CDs) has been widely known due to their outstanding property on tunable fluorescence emission influenced by the different functional groups, heteroatom doping and surface passivation (Saengsrichan et al., 2022b; Sakdaronnarong et al., 2020; Sangjan et al., 2022). Owing to the excellent fluorescence emission property of CDs, a previous work reported that CDs was easily formed a network in calcium alginate gel was used as tetracycline adsorber and exhibited a quenching fluorescence property when binding with tetracycline, therefore the CDs/alginate gel bead was successfully utilized as fluorometry sensing agent of tetracycline (Ehtesabi et al., 2019). Lately, it has been reported that CDs exhibited excellent reactive oxygen species (ROS) regulate properties which could be applied as antimicrobial agent, nanomedicine and therapeutics (Li et al., 2023; Zhao et al., 2023). Organic-loaded CDs and metal/CDs nanocomposite were reported to play a vital role on controlling microbial growth especially on the stage of biofilm formation (Liu et al., 2022; Wang et al., 2019a). Due to its photo-responsive property of CDs to generate ROS (Sakdaronnarong et al., 2020), the application on antimicrobial and microorganism inactivation effect have been intensively studied (Li et al., 2022; Wu et al., 2022). The research conducted by Zhang et al. revealed a correlation between the photo-oxidation activity, phosphorescent quantum yield, and nitrogen (N) content of CDs. This highlights the significance of N-doping in enhancing the photosensitization performance of CDs (Zhang et al., 2018). When exposed to visible or natural light, CDs in a direct contact with bacterial cells have the ability to efficiently generate ROS by activating oxygen present in the air or water. This process results in the production of hydroxyl free radicals ($OH^{\bullet}$) and/or singlet oxygen ($^1O_2$), which can cause damage to essential biomolecules within the cell and ultimately lead to cell death (Dong et al., 2020). Mechanism of ROS generation could be influenced by exogenous light irradiations to enable controllable ROS generation for photodynamic therapy (PDT) or inorganic nanozymes with peroxidase-like activities can convert endogenous biological H_2O_2 into highly cytotoxic $\bullet OH$ for chemodynamic therapy (CDT). Accordingly, a previous work disclosed antimicrobial activity of N and S doped CDs prepared from poly (sodium- 4-styrene sulfonate) or polyvinylpyrrolidone due to the chemical interaction of surface electrostatic charge of carbon dots toward cell membrane of bacteria (Travlou et al., 2018).

There have been limited studies on the combination of MSN and CDs, with only a few existing research papers for the application of metal detection (Wang et al., 2019b), drug delivery, bioimaging (Zhao et al., 2017) and gas sensing (Wang et al., 2016). Furthermore, the utilization of CDs/MSN composites for antimicrobial and anti-biofilm activity has been rare (Liu et al., 2017). Although, there have been the studies on polymer composite of carbon dot using physical crosslinking process for polyvinyl alcohol/CDs (PVA/CDs) composite (Hu et al., 2016) and chemical crosslinking agent e.g., EDC/NHS for polyvinyl pyrrolidone/CDs (PVP/CDs) composite (Nayak et al., 2020). It still needs to be researched on an appropriate approach after conjugation of CDs with MSN to formulate the excellent distribution of nanocomposite inside the polymer matrix. As a result, there is a need for further investigation and more studies in this area to explore and expand the potential applications of these composites for either bacterial infection treatment or biofilm formation control and other related fields.

Therefore, in the present study, the effect of photo-responsive characteristics of carbon dot conjugated on MSN on antimicrobial and antibiofilm activity was studied and discussed herein. A combination of organic substance doping namely N and S doped carbon dots on MSN (NS/CDs@MSN) and neat carbon dots on MSN (CDs@MSN) nanocomposite in PVA hydrogel matrix on antimicrobial activity and cytotoxicity toward fibroblast cells (L-929 and NIH/3 T3) was determined. The role of the thermo-physical crosslinking process that influences the surface chemistry, photonic characteristics of the heteroatom carbon dots/MSN nanocomposite as well as thermal degradation, phase transition and crystallinity of carbon dots/MSN/PVA composite hydrogel was then extensively analyzed and linked to the antibacterial capability and cytotoxicity of the materials.

2. Materials and methods

2.1. Materials and chemicals

Palm empty fruit bunch (EFB) was contributed from a palm oil refinery plant, Thailand. EFB was washed, dried, and milled to approximately 75–300 μm (+50/−200 mesh). Sodium thiosulfate and anhydrous ethyl alcohol (99.9%) were purchased from Daejung, Korea. *P*-phenylenediamine and diethanolamine were supplied from Alfa Aesar, Germany. Tetraethyl orthosilicate (TEOS) was obtained from Acros organics, Germany and acetone was purchased from Fisher chemical, USA. Cetyltrimethyl ammonium bromide (CTAB) was acquired from Sigma-Aldrich, USA. Ultrapure water was purified by a New
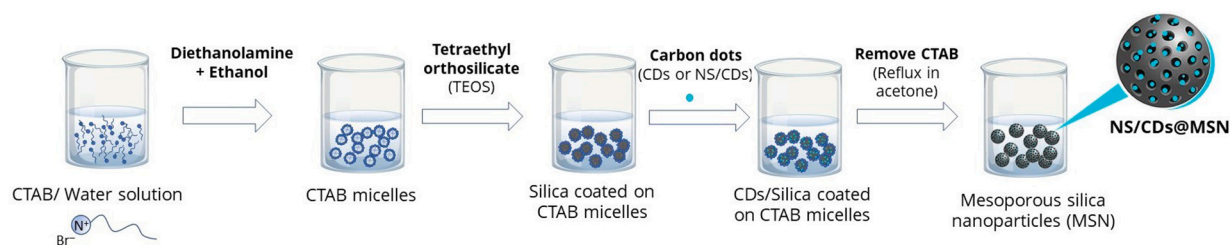
Scheme 1. Schematic illustration of the preparation of mesoporous silica nanoparticles (MSN) and CDs@MSN or NS/CDs@MSN nanocomposites

Human UP System, Korea (18.3 MΩ cm at 25 °C). For MTT assay, Dulbecco's modified Eagle's medium (DMEM; high glucose, pyruvate, powder), minimal essential medium α (MEM; nucleosides, powder), fetal bovine serum (FBS), and antibiotic-antimycotic (anti-anti) were purchased from Gibco (Billings, MT, United States). Dimethyl sulfoxide (DMSO), sodium bicarbonate, and thiazolyl blue tetrazolium bromide (MTT) were purchased from Sigma-Aldrich Inc. (Darmstadt, Germany). PBS 10× was obtained from Omics Bio (New Taipei City, Taiwan). All chemicals were used as received. L-929 and NIH/3 T3 cell lines were obtained from the National Health Research Institutes (Miaoli, Taiwan).

2.2. Methodology

2.2.1. The synthesis of carbon dots (CDs) and N,S doped carbon dots (NS/CDs)

A single step hydrothermal method was used to synthesize CDs from EFB. 2.5 g EFB was mixed with ultrapure water at 1:20 of solid: liquid ratio (w/w) in a Teflon-lined high-pressure reactor. The reaction took place at 220 °C for 6 h and then cooled down to room temperature naturally. The solid fraction was separated using centrifugation at 11,000 rpm for 20 min and brown solution containing CDs was purified using microfiltration with a 0.22 μm filter membrane and further dialyzed by using membrane (MWCO 1.0 kDa) for 48 h. For nitrogen and sulfur doped CDs (NS/CDs), *p*-phenylenediamine and sodium thiosulfate were used respectively. The N- and S-doping agents at different concentration from 0.20 mol L^{-1} to 0.40 mol L^{-1} were mixed with EFB at the same solid: liquid ratio. The CDs and NS/CDs synthesis procedure of our group and the characterization were reported elsewhere (Saengsrichan et al., 2022a; Saengsrichan et al., 2022b; Sangjan et al., 2022). The CDs and NS/CDs samples were stored at 4 °C for further use and characterization.

2.2.2. Synthesis of mesoporous silica nanoparticles (MSN) and in-situ CDs@MSN nanocomposite

To synthesize MSN, SiO_2 nanoparticles were firstly formed by mixing of 7 mL ethanol, 50 μL diethanolamine and 10 mL ultrapure water with 0.2 g CTAB, and subsequently the solution was stirred at 60 °C for 30 min. After 0.5 h, 2 mL TEOS was rapidly added and the mixture was maintained stirring for further 2 h. After the reaction, silicon dioxide nanoparticles (SiO_2) were obtained from centrifugation at 8,000 rpm for 5 min and the precipitate was dried in an oven at 60 °C overnight. For *in-situ* CDs@MSN nanocomposite, CDs solution from the previous step was added instead of ultrapure water during CDs@SiO_2 synthesis. In order to obtain porous reduced MSN or CDs@MSN nanocomposite, the prepared SiO_2 or CDs@SiO_2 nanoparticles were taken into a three-neck round bottom flask, then 100 mL acetone was added and the reduction took place at 80 °C under reflux for 18 h. After centrifugation at 8,000 rpm for 5 min, the final products (MSN or CDs@MSN) were dried at 60 °C for 24 h. In case of NS/CDs@MSN, the prepared NS/CDs solution was added instead of CDs solution. All the MSN, CDs@MSN and NS/CDs@MSN samples were stored in an auto-desiccator (25% relative humidity) for further use and characterization. The method for *in-situ* synthesis of MSN, CDs@MSN or NS/ CDs@MSN nanocomposite was shown in Scheme 1.

2.2.3. Synthesis of CDs@MSN/PVA composite hydrogel

The neat PVA hydrogel and CDs@MSN/PVA composite hydrogel were fabricated using the repeatedly freezing–thawing technique (Hajidariyor et al., 2023). The CDs@MSN/PVA composite hydrogels containing 24 wt% PVA (W_{PVA}/W_{all}) and different CDs contents were prepared. The CDs, NS/CDs, CDs@MSN and NS/CDs@MSN samples were dispersed in ultrapure water at 4 wt% (W_{CDs}/W_{PVA}) CDs content. As an example, 24 g of PVA powder and 19.2 mL of CDs or CDs/MSN solution were mixed and poured into 76.8 mL ultrapure water while stirring at 45 °C, and the solution was continued stirring for 30 min. Subsequently, PVA was completely dissolved at 95 °C at the stirring speed of 200 rpm for 2 h. Finally, the transparent homogeneous CDs@PVA or CDs/MSN@PVA suspension was obtained. Afterward, the homogeneous CDs@PVA or CDs/MSN@PVA suspension was vacuumed at 40 °C for air bubbles removal. To fabricate the PVA hydrogel, the degassed mixture was poured into a polystyrene petri dish or cylindrical silicone mold. The CDs@PVA or CDs/MSN@PVA suspension was subjected to repeatedly freezing–thawing cycles (a freezing step for 18 h, at −20 °C followed by a thawing step for 6 h at room temperature). The cycles of freeze-thaw were repeated until the CDs@PVA or CDs/MSN@PVA composite hydrogels were formed (ca. 15 cycles).

2.2.4. Antimicrobial activity of CDs@MSN and CDs/MSN@PVA hydrogel

For synthesized CDs and CDs@MSN nanoparticles, antimicrobial susceptibility study against the growth of *Staphylococcus aureus* (ATCC 25923), *Escherichia coli* (ATCC 25922) and *Pseudomonas aeruginosa* (ATCC 27853) was studied using a disk diffusion method. The result of diameter of inhibition zone (mm) was measured with three replicates. Minimum inhibitory concentration (MIC) and minimal bacteria concentration (MBC) of all microorganisms tested were measured using a broth dilution method. All the methods used in this study followed M100 Performance Standards of Clinical and Laboratory Standards Institute (CLSI) (30th Edition, 2020).

To investigate the antibacterial activity of hydrogel against *Staphylococcus aureus* ATCC 25923 which is the major bacteria found in acute and chronic wound, the bacteria was cultured in Fresh Tryptone Salt Broth (TSB) medium at 37 °C under shaking and aerobic condition until the optical density (OD600) of bacteria suspension was 0.75 ± 0.01 at 620 nm. The CDs/MSN@PVA, NS/CDs/MSN@PVA hydrogels and all the controls were sterilized under the UVC irradiation for 10 min prior to place onto the center of culture plates of *S. aureus* which were prepared by adding Mueller–Hinton (GMH) agar (15 g L^{-1}) to PBS medium and 1 mL of *S. aureus* suspension after the agar was solidified. The culture plates were incubated at 37 °C overnight in aerobic condition under daylight from a fluorescence lamp 36 W, 2850 Lumens (TL-D-36 W-PHILIPS Daylight, Philips, Japan) with the distance of ~75 cm between light source and the samples. The presence of clear zone which indicated the inhibited biofilm formation and bacterial growth was measured for 4 positions per plates and the experiment was done triplicates.

2.2.5. Study on anti-biofilm formation activity of CDs@MSN and CDs/MSN@PVA hydrogel

To quantity biofilm formation of *Staphylococcus aureus* ATCC 25923, the protocol was performed by using microplate assay as previously

described (Cassat et al., 2007) with some modifications. A colony of *S. aureus* was inoculated in TSB supplemented with 1% Glucose and incubate at 37 °C, 200 rpm, overnight (16 h). The overnight culture was diluted to 0.5 McFarland concentration with biofilm medium (TSB supplemented with 1% Glucose). 200 μL of diluted culture was transferred into 96 well of microplate and incubated at 37 °C for 24 h without shaking under daylight from a fluorescence lamp 36 W, 2850 Lumens (TL-D-36 W-PHILIPS Daylight, Philips, Japan) with the distance of ~75 cm between light source and the samples. Culture broth was discarded by gentle aspiration. The wells were washed one time with 200 μL of sterile phosphate buffer saline (PBS) to remove non-attached biofilm. And then the attached biofilm was fixed with 200 μL of 100% ethanol at room temperature for 20 min. After ethanol was removed, the plate was dried with the lid off in a sterile hood for 20 min. Subsequently, 200 μL of 1% of crystal violet was added into the wells to stain biofilm for 8 min (Shi et al., 2019) and the crystal violet was discarded by gentle aspiration. Next, the wells were washed with 200 μL of tap water for two times to remove the excess staining and dried overnight. The crystal violet in the wells was dissolved with 200 μL of 30% acetic acid and measured at OD_{560} by using the microplate reader (Cytation5 imaging reader, Bio-Tek, USA) (Supa-Amornkul et al., 2019).

2.2.6. Cytotoxicity study

MTT assay was used to investigate the cytotoxicity of CDs and hydrogel samples. The MTT assay of the hydrogels was performed using an extraction method mentioned in ISO-10993-5-2009. NIH/3 T3 cells were cultured in DMEM supplemented with 10% FBS and 1% anti-anti. L-929 cells were cultured in MEM α supplemented with 10% FBS and 1% anti-anti.

For extraction of the hydrogel samples, the hydrogels were cut, weighted, and soaked in the complete culture medium at a concentration of 1 mg mL^{-1}. The mixture was stored in a 10-cm petri dish and incubated for 1 day in a 37 °C incubator with 5% CO$_2$. After 24 h, the extract was ready for the MTT assay.

For MTT assay, 100 μL of the complete culture medium containing L-929 cells (1×10^5 cells mL^{-1} in DMEM) or NIH/3 T3 cells (1×10^5 cells mL^{-1} in MEM α) which are mouse fibroblast cell lines obtained from the National Health Research Institute, Taiwan was seeded into the well of a 96-well plate and incubated in a 37 °C incubator with 5% CO$_2$. After 24 h of cultivation, the culture medium was removed and replaced with the CDs solution or hydrogel extracts. Different concentrations of the CDs solution or hydrogel extract (ranged from 0 to 100%) were tested by diluting the aliquot sample with culture medium. After another 24 h of culture, the culture medium containing CDs solution or hydrogel extract was removed, and the cells were rinsed 2 times with 100 μL of PBS. Then, 100 μL of the MTT reagent were added to the well, and the cells were incubated for 2 h. The MTT reagent was prepared by diluting the stock solution of MTT in PBS (5 mg mL^{-1}) 10 times with serum-free culture medium. After the incubation, the MTT reagent was removed, and 100 μL of the DMSO was added to the well to dissolve the formazan. The 96-well plate was shaken for at least 10 min on an orbital shaker. Finally, the absorbance of the solution at 570 nm was read with a PerkinElmer EnSpire™ microplate reader. The blank reading (using 100 μL of DMSO in the well) was first subtracted from the reading of the samples. And the cell viability (%) was calculated using the eq. (1).

$$Cell\ Viability\ (\%) = \frac{Absorbance\ of\ the\ sample}{Absorbance\ of\ the\ control} \times 100 \qquad (1)$$

2.2.7. Characterizations

Crystal structure of nanomaterial (CDs@MSN, NS/CDs@MSN and MSN) and PVA composite hydrogel was characterized using X-ray diffractometry (XRD) (Gupta et al., 2009) with 2-theta from 10 to 50 degrees (D8 Discover Model, Bruker, Germany). The FTIR spectrum of samples was tested in the range of 400–4000 cm^{-1} with NICOLET iS50 FTIR spectrometer (Model Nicolet iS50 FTIR, Thermo Scientific, USA)

using diamond tablet. The qualitative and quantitative investigation of chemical constituents of samples was carried out by means of X-ray fluorescence (XRF) (Horiba Scientific, France). Field Emission Scanning Electron Microscope (FESEM) equipped with a field emission electron gun of 5 kV was used to analyze morphology of nanoparticles. Zeta potential measurement and hydrodynamic diameter determination of nanoparticles were done triplicates for each sample by a zetasizer (Malvern Panalytical, Japan). The absorbance of NS/CDs@MSN was measured using UV-1800 UV–Vis double beam spectrophotometer (Model UV-1800, Thermo Fisher Scientific, Japan) with the scanning wavelength range between 200 and 800 nm. Fluorescence measurement of NS/CDs@MSN was performed on a Spectrofluorometer (Model FP-6200, Perkin Elmer, Japan). The fluorescence behavior was studied by varying an excitation wavelength in a range of 270–370 nm with a 10 nm increment. Surface area, pore size distribution and pore volume of prepared nanoparticles were determined by the N$_2$ adsorption-desorption using the Brunauer-Emmett-Teller (BET) mehod (Micromeritics ASAP 2000, Sweden). The nano-size, layer and size contribution of particles was observed by Field emission transmission electron microscope with accelerating voltage of 300 kV (FETEM, Model JEM-3100F, JEOL, Japan). The elemental composition of the samples was analyzed using X-ray photoelectron spectroscopy (XPS) at the SUT-NANOTEC-SLRI Joint Research Facility, Synchrotron Light Research Institute (SLRI), Thailand. The PHI5000 VersaProbe II (ULVAC-PHI, Japan) instrument was employed for this purpose. The specimens were excited by a Monochromatized Al-Kα X-ray source (with hγ = 1486.6 eV). Thermal degradation rate of PVA hydrogels were analyzed using Thermogravimetric analysis (TGA) (NETZSCH, STA 449 F3 Jupiter, Germany) under nitrogen atmosphere at 10 °C min^{-1} scan rate from room temperature (30 °C) to 800 °C. Phase transition of glass transition, melting point and crystallization of hydrogel were characterized by Differential scanning calorimetry (DSC) (DSC 214 Polyma, Netzsch, USA) at 10 °C min^{-1} scan rate from −40 to 260 °C under 40 mL min^{-1} nitrogen flow rate.

3. Results and discussion

3.1. Synthesis and characterization of CDs, NS/CDs and CDs@MSN nanocomposites

The XRD patterns of four mesoporous silica nanoparticles before and after reflux were presented in Fig. S1. The findings revealed that a broad diffraction peak was emerged at 22° in all CDs@SiO$_2$, NS/CDs@SiO$_2$, CDs@MSN and NS/CDs@MSNs samples representing typical peak of amorphous carbon which was overlapped with peak of amorphous carbon (Baig et al., 2021). However, prior to reflux the sharp peaks of crystalline SiO$_2$ were appeared at 21.5° and 24.5°. After reflux with acetone to enhance porosity of silica particles, the crystalline peaks via XRD patterns of all SiO$_2$ disappeared indicating enhanced amorphous structure of silica in CDs@MSN, 0.20 M NS/CDs@MSN, 0.40 M NS/CDs@MSN and MSN as shown in Fig. S1(B), which indicates the existence of amorphous silica presence in MSN nanoparticles (Sadek et al., 2013). In case of carbon dots/silica nanocomposite prior to reduction reaction under reflux as demonstrated in Fig. S1(A), the XRD intensity of broad peak at 22° of all samples were less than those of samples after reflux (Fig. S1(B)). This was possibly due to the higher purity of silicon dioxide was achieved in MSN samples. In other words, the phase of silica was more stable in spite of combining with CDs or after refluxing and noted that no contamination of other metals was found in XRD patterns, thus the result confirms the innocence of SiO$_2$ in all MSN nanocomposites.

FTIR spectra of NS/CDs@SiO$_2$ before reflux and NS/CDs@MSN after reflux at 80 °C are shown in Fig. S2(A) and S2(B), respectively. Fig. S2 (A) shows the FTIR band located at 433.34 cm^{-1} which was attributed to the Si − O stretching vibration which could be attributed to O-Si-O/Si-O-Si bending vibration while peaks located at 720 cm^{-1} and 789.40 cm^{-1}
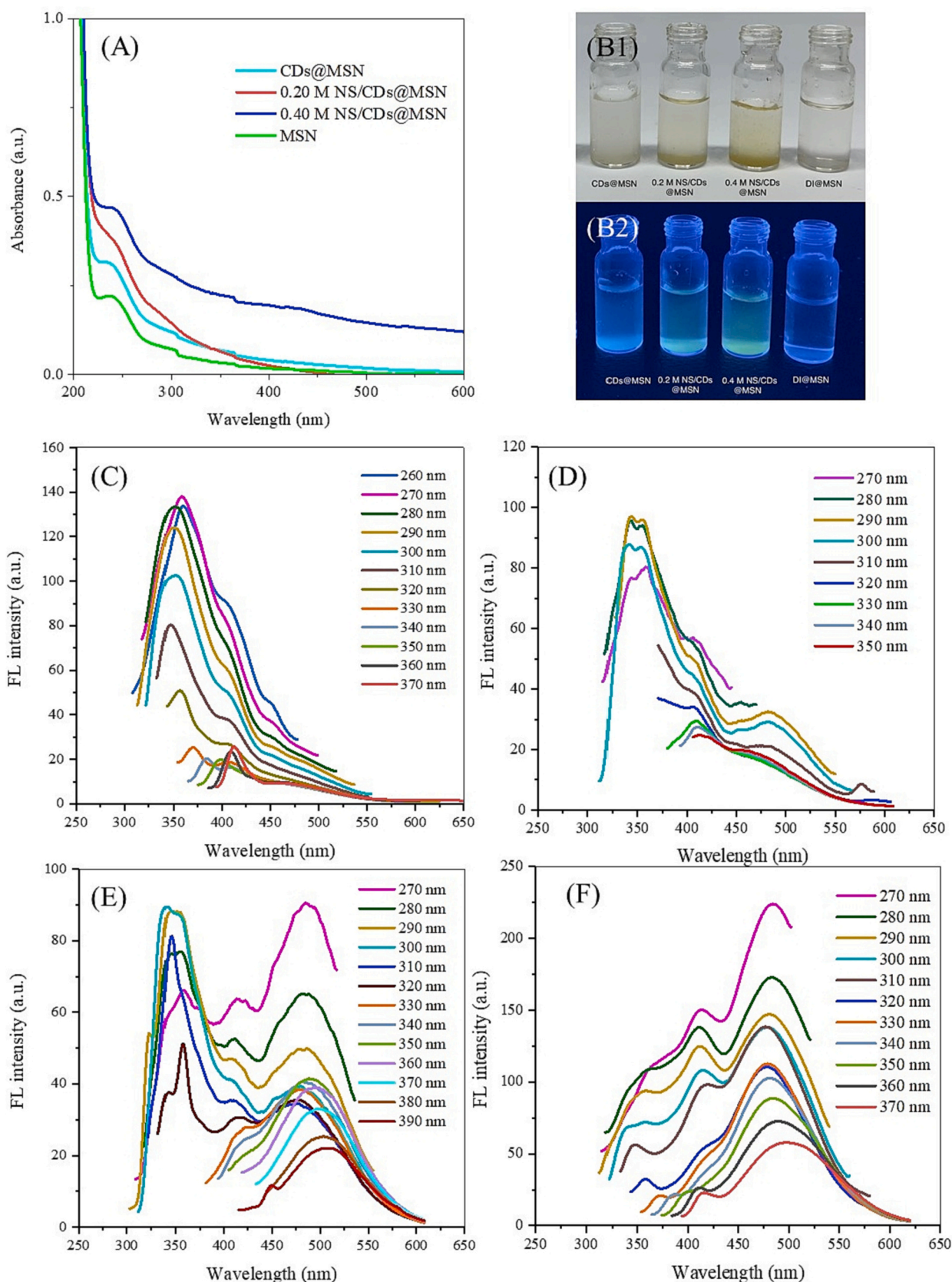
Fig. 1. (A) UV–Vis absorption spectra of CDs@MSN, 0.20 M NS/CDs@MSN, 0.40 M NS/CDs@MSN, and MSN; (B) Photographs of samples (B1) under natural light and (B2) under UV at 365 nm; Fluorescence intensity of (C) MSN, (D) CDs@MSN, (E) 0.20 M NS/CDs@MSN, and (F) 0.40 M NS/CDs@MSN when the excitation wavelength varied from ~270 to ~370 nm.

were due to either the Si − OH stretching vibration (King et al., 2004) or Si − O bond vibration in silica (SiO$_2$) which was noted at 1100/1200 and 810 cm^{-1} (Yusuf, 2023). Besides, the presence of stretching Si − O − Si was demonstrated at 1042.33 cm^{-1} while those at 3300.67 cm^{-1}, 1629.93 cm^{-1}, and 1466.08 cm^{-1} can be assigned to the hydroxyl group (O − H) stretching vibration. The FTIR peaks of CTAB (2920.82 cm^{-1}, 2851.23 cm^{-1}) were prominent for SiO$_2$ nanoparticles (Deng et al., 2008) as shown in Fig. S2(A). In contrast, CTAB peaks slightly reduced for MSN nanocomposites after reflux reaction in acetone (Fig. S2(B)). The FTIR peaks revealed that CTAB-template for MSN synthesis was somewhat removed due to the absence of CTAB functional groups on the refluxed MSN sample. However, the FTIR peaks for the −CH$_2$−, N (CH$_3$)$_2$, −CH− groups at around 2851.23 cm^{-1} corresponding to C—H stretching vibration still remained in MSN sample after reflux, therefore it can be seen that CTAB surfactant has decreased but not completely disappeared. The results agreed with atomic concentration data from XPS analysis shown in Table S1 in which neat MSN still contained some amount of carbon atoms after synthesis. Besides, many more surface hydroxyl groups can also be observed in MSN. This could possibly enhance the hydrophilic property of MSN and could modify the reactive capability of pore channels formed inside MSN.

Photo-responsive properties of CDs@MSN, 0.20 M NS/CDs@MSN, 0.40 M NS/CDs@MSN, and MSN (control) were investigated by UV–Vis spectroscopy and fluorescence (FL) spectrophotometry. Fig. 1(A) displays the UV–Vis absorption of CDs@MSN and all NS/CDs@MSN nanocomposites as well as MSN in a range of 200 to 500 nm. The UV–Vis profile demonstrates a specific absorption peak at ~240 nm of all nanoparticles which is related to the π - π * transition of electrons in the conjugated C=C bond of carbon nanostructure. The UV–Vis absorption spectrum of the silica nanoparticles was reported at around 260–270 nm, however the intensity of MSN itself was not obvious (Zhao et al., 2016). A previous report additionally disclosed an unobvious absorption shoulder of silica nanoparticles at around 260 nm (Chen et al., 2013). The shoulder observed was possibly due to the absorption of C − H bonds on MSN surface from incomplete removal of CTAB. In case of nitrogen and sulfur doped carbon dots, the absorption peak in a range of 230–350 nm was observed which corresponds to the n − π* transition of C—N, C=N, and C=O bonds (Ding et al., 2020; Liu et al., 2019b; Sahiner et al., 2019). Therefore, 0.40 M NS/CD@MSN showed highest UV-Vis absorbance while the low-intensity absorption of n → π* of MSN was presumably caused by the lowest content of N and S, along with weak electron transition of the functional groups of CDs inside the mesoporous silica nanoparticles.

Figure 1(B) displays the photograph of the solution of MSN, CDs@MSN and all NS/CDs@MSN samples under natural light (Fig. 1 (B1)) and under UV at λ = 365 nm (Fig. 1(B2)) showing a good corresponding result with fluorescence (FL) spectroscopy in Fig. 1(C) to 1(F). The results revealed that the emission wavelength was independent on the excitation wavelength for both MSN and CDs. As shown in Fig. 1(C), MSN gave high fluorescence emission when excited with laser between λ$_{Ex}$ = 260 nm and λ$_{Ex}$ = 280 nm while the emission wavelength of MSN was at ~350–370 nm indicating particles with blue-emitting characteristics. The result is in good accordance with a previous research (Chen et al., 2013), however the blue-shifting of emission wavelength from 500 nm (λ$_{Ex}$ = 380–400 nm) in the previous study to 350–370 nm (λ$_{Ex}$ = 260–280 nm) in the present study was possibly due to either the difference in surface functional groups which still contained CTAB molecules or the effect of quantum confinement from the smaller size of synthesized MSN which was 80–100 nm in the previous study compared with 26.73 ± 3.50 nm for FETEM image analysis of MSN in the present study (Fig. 5(D)). After forming nanocomposite with CDs, Fig. 3(D) depicts an appearance of FL emission peaks of MSN at ~350 nm and that of CDs at ~480–500 nm when excited at wavelength of 290 to 300 nm. This exhibits phenomenon of surface plasmon resonance effect of transporting electron between silica nanoparticles and carbon dots. Similarly, two prominent FL emission peaks occurred for 0.20 M NS/

Table 1
Zeta potential, BET surface area, BJH pore volume and pore diameter of CDs@MSN and NS/CDs@MSN samples.

Sample	Zeta potential (mV)	S$_{BET}$ surface area (m^2 g^{-1})	BJH Pore volume (cm^3 g^{-1})	BET Pore size (nm)
CDs@MSN	53.9	40.21	0.52	8.24
0.20 M NS/CDs@MSN	−37.8	62.89	0.57	13.43
0.40 M NS/CDs@MSN	6.4	47.89	0.56	12.95
MSN	28.7	71.82	0.77	12.81

CDs@MSN at λ$_{Em}$ = 330–350 nm (blue emission) and λ$_{Em}$ = 480–500 nm (green emission) when excitation (λ$_{Ex}$) wavelength was between 270 and 300 nm (Fig. 3(E)). Nevertheless, when using longer excitation wavelength near visible light (330 nm to 390 nm), only FL emission of NS/CDs was detected and no FL emission of MSN was observed. Even more, FL emission intensity of 0.40 M NS/CDs@MSN in Fig. 1(F) demonstrated solely the resultant emission from N- and S- doped carbon dot at wavelength of 480–500 nm with high intensity and no obvious emission of MSN was observed. The result of emission wavelength between 480 and 500 nm from 0.20 M NS/CDs@MSN and 0.40 M NS/CDs@MSN exhibited good corresponding consequences to green emitting agent as illustrated in Fig. 1(B) under UV excitation at 365 nm similar to a previous work (Liu et al., 2019b). To sum up, the low concentration of N,S doped CDs@MSN i.e., 0.20 M NS/CDs@MSN had no effects on excitation and emission wavelength of MSN, while high amount of N, S doped CDs onto MSN nanocomposite played a major role to exhibit red-shift phenomenon, thus excitation wavelength was shifted from blue emission at λ$_{Ex}$ = 270–290 nm to green emission at a broad range of excitation λ$_{Ex}$ = 300–370 nm which was near natural or white light range(Song et al., 2020; Sun et al., 2013). The results from the present work confirmed that the presence of N and S heteroatoms in carbon dots considerably resulted in higher FL properties for longer wavelength emissive (blue to green) characteristics (Saengsrichan et al., 2022b).

The surface charge expressed as zeta potentials of the CDs@MSN, 0.20 M NS/CDs@MSN, 0.40 M NS/CDs@MSN and neat MSN was determined as 53.9 mV, −37.8 mV, 6.4 mV and 28.7 mV at pH = 7, respectively, as demonstrated in Table 1. The electrostatic charge of silica layer of MSN demonstrated positively charged which was similar to a previous study (Hao et al., 2017) and thus MSN could form nanocomposite with CDs resulting in CDs@MSN nanocomposite with stronger positively charged. The 0.20 M NS/CDs@MSN sample had greatly negative charge possibly due to the presence of Si–COOH as well as –Si–OH groups on the surface that dominated the lower content of N and S dopants providing positive charge. The neutral surface charge of 0.40 M NS/CDs@MSN was obtained which was possibly because of positive charge of nitrogen, sulfur as well as SiO groups coated on CDs@MSN surface. The zeta potential of silica nanoparticles is very sensitive in different pH; it has been reported that at the pH higher than seven, the zeta potential presumably continues positive (Sheng et al., 2022). The difference in highly negative charge of 0.20 M NS/CDs@MSN and highly positive charge of CDs@MSN was mainly led to the distinct binding efficiency among these nanocomposites toward targeted molecules or unique molecular structure of microorganisms for antibacterial application.

Apart from surface charge of nanoparticles, surface area, micro-pore volume and pore diameter were particular characteristics of nanocomposites that render to enhance their performance to adsorb the target molecules or loading capacity for trapping or encapsulating small molecules. As demonstrated in Table 1, surface area and pore volume of MSN was highest at 71.82 m^2 g^{-1} and 0.77 cm^3 g^{-1}, respectively compared with CDs@MSN (40.21 m^2 g^{-1} and 0.52 cm^3 g^{-1}), 0.20 M NS/CDs@MSN (62.89 m^2 g^{-1} and 0.57 cm^3 g^{-1}) and 0.40 M NS/CDs@MSN
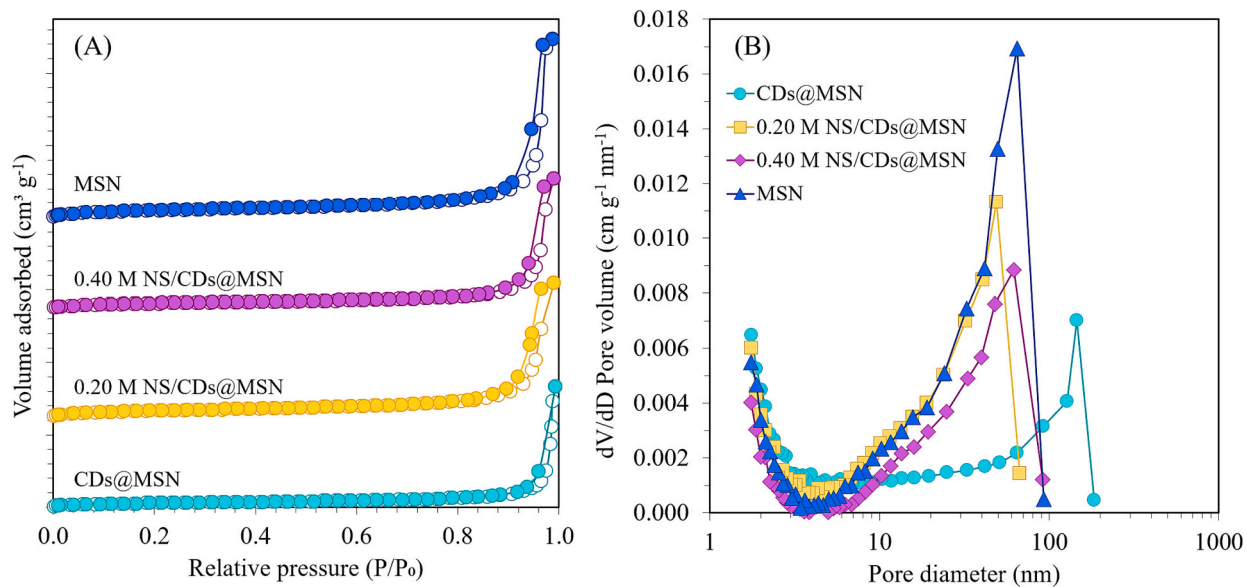
Fig. 2. (A) the relationship between relative pressure (P/P₀) and adsorbed volume of nitrogen gas, and (B) the plots of dV/dD pore volume versus pore diameter during adsorption of CDs@MSN, 0.20 M NS/CDs@MSN, 0.40 M NS/CDs@MSN and MSN samples.
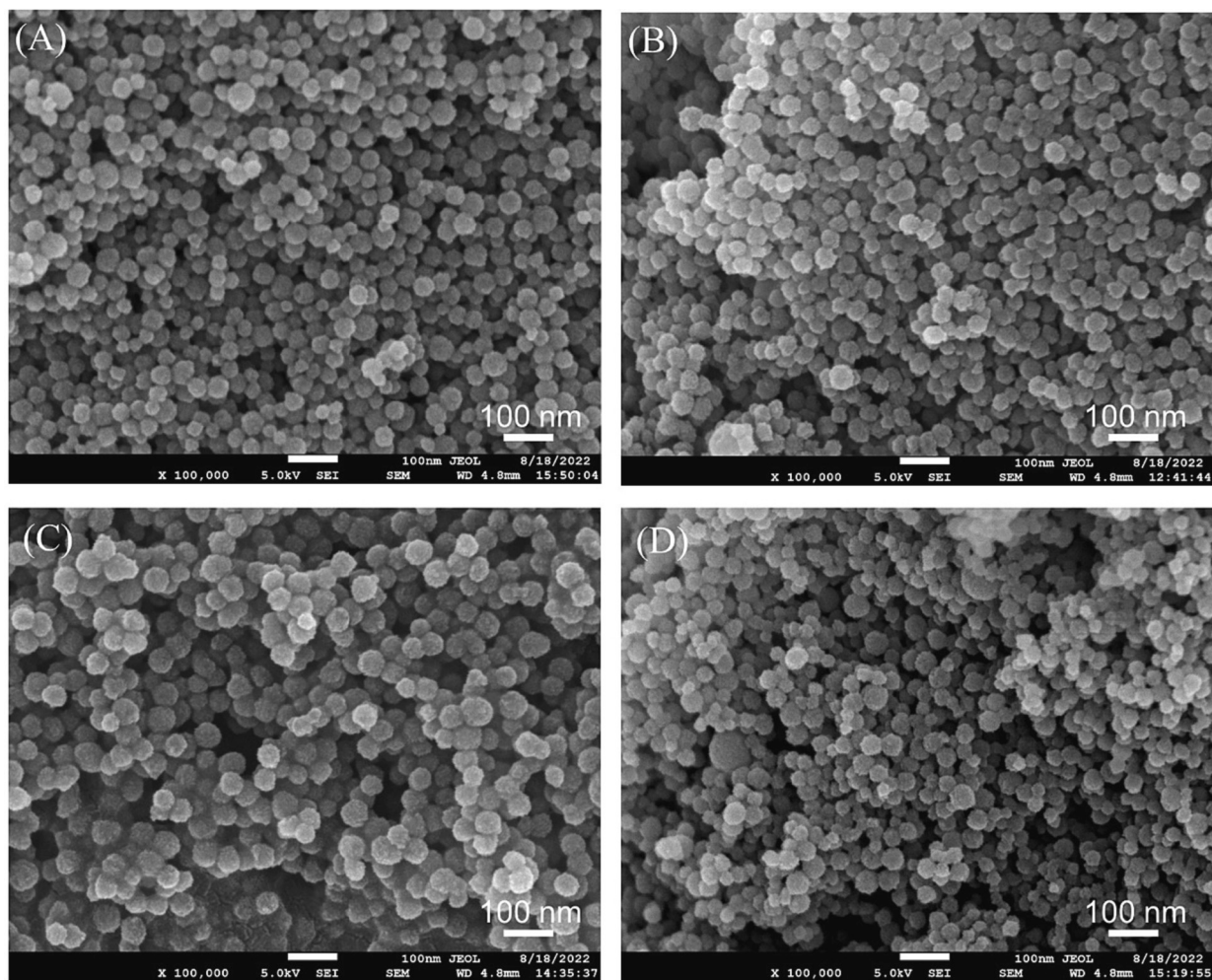

Fig. 3. FESEM imaging of different samples: (A) CDs@MSN, (B) 0.20 M NS/CDs@MSN, (C) 0.40 M NS/CDs@MSN, and (D) MSN after reflux in the form of mesoporous silica nanoparticles.
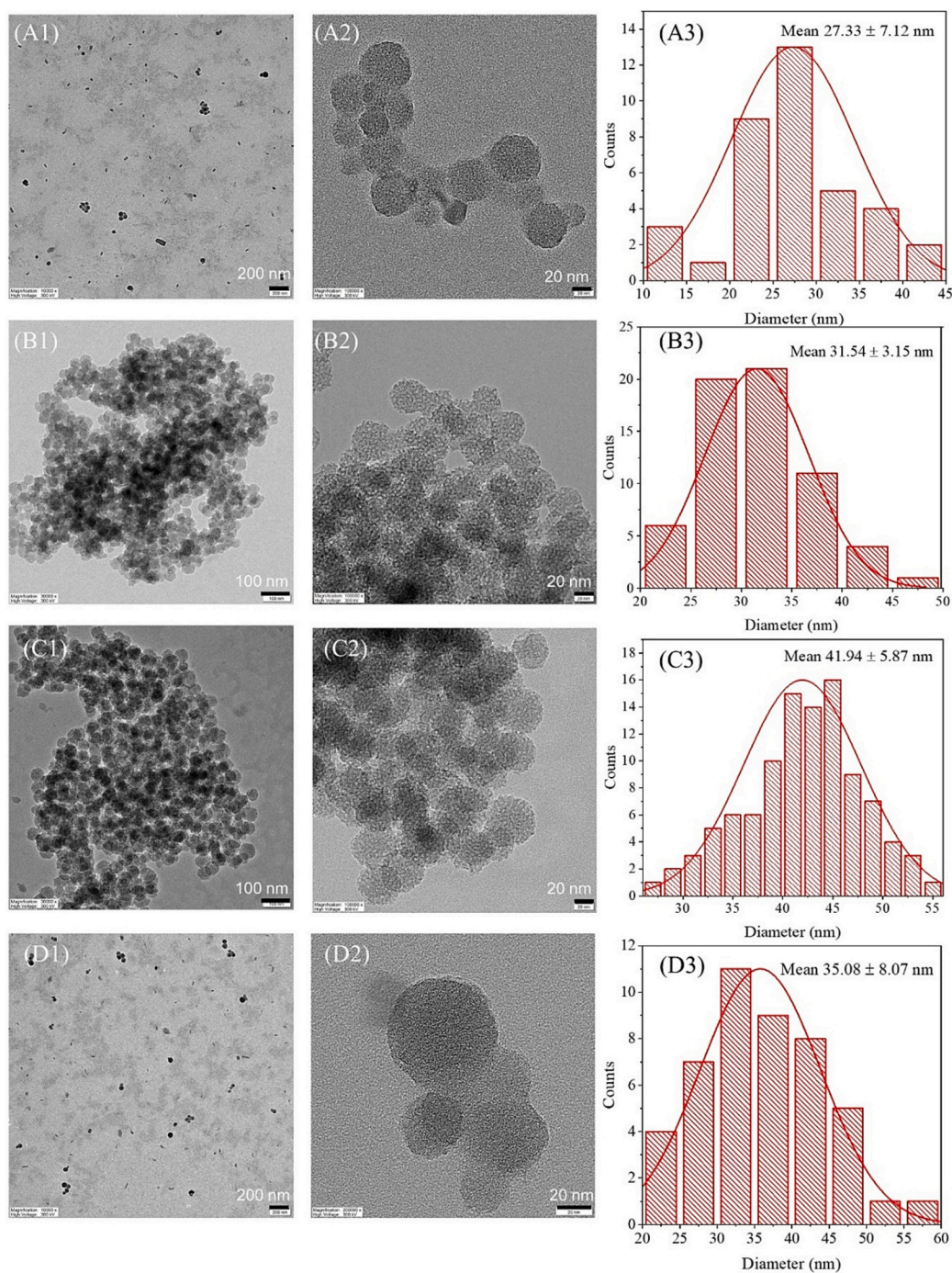
Fig. 4. FETEM imaging of different samples: (A) CDs@SiO$_2$, (B) 0.20 M NS/CDs@SiO$_2$, (C) 0.40 M NS/CDs@SiO$_2$, and (D) SiO$_2$ before reflux in the form of SiO$_2$ when 1) FETEM images at 10,000× or 30,000× magnification, 2) FETEM images at 100,000× magnification, and 3) average diameter and size distribution of nanoparticles.

(47.89 m^2 g^{-1} and 0.56 cm^3 g^{-1}). The result was conceivable because carbon dots were included into the MSN pore and this may cause a reduction of pore volume and thus surface area of nanocomposites. A significant decrease of average pore size from 12.81 nm to 8.24 nm was presumably due to smaller size of CDs relative to NS/CDs which could penetrate into MSN pore and therefore influenced the decline of pore size of CDs@MSN sample.

The relationship between relative pressure (P/P$_0$) and adsorbed volume of nitrogen gas as well as the change of dV/dD according to pore volume were presented in Fig. 2(A) and 2(B), respectively. The isothermal adsorption and desorption curves of CDs@MSN, 0.20 M NS/

CDs@MSN, 0.40 M NS/CDs@MSN, and MSN in Fig. 2(A) illustrate similar patterns. Since silica porous materials are extensively described as materials that possess pores spanning multiple length scales, including macro-pores (larger than 50 nm), meso-pores (ranging from 2 to 50 nm), and micro-pores (<2 nm) in size (Guerritore et al., 2022), the dV/dD pore volume analysis from Fig. 2(B) showed that micro-pore diameter was found in all MSN nanocomposite at <2 nm pore diameter. In addition, the micro-to-macro pore diameter distribution of CDs@MSN was also observed in a range of 100 and 150 nm while those of 0.20 M NS/CDs@MSN, 0.40 M NS/CDs@MSN, and MSN samples were found in a range of 10 and 80 nm. The findings provided
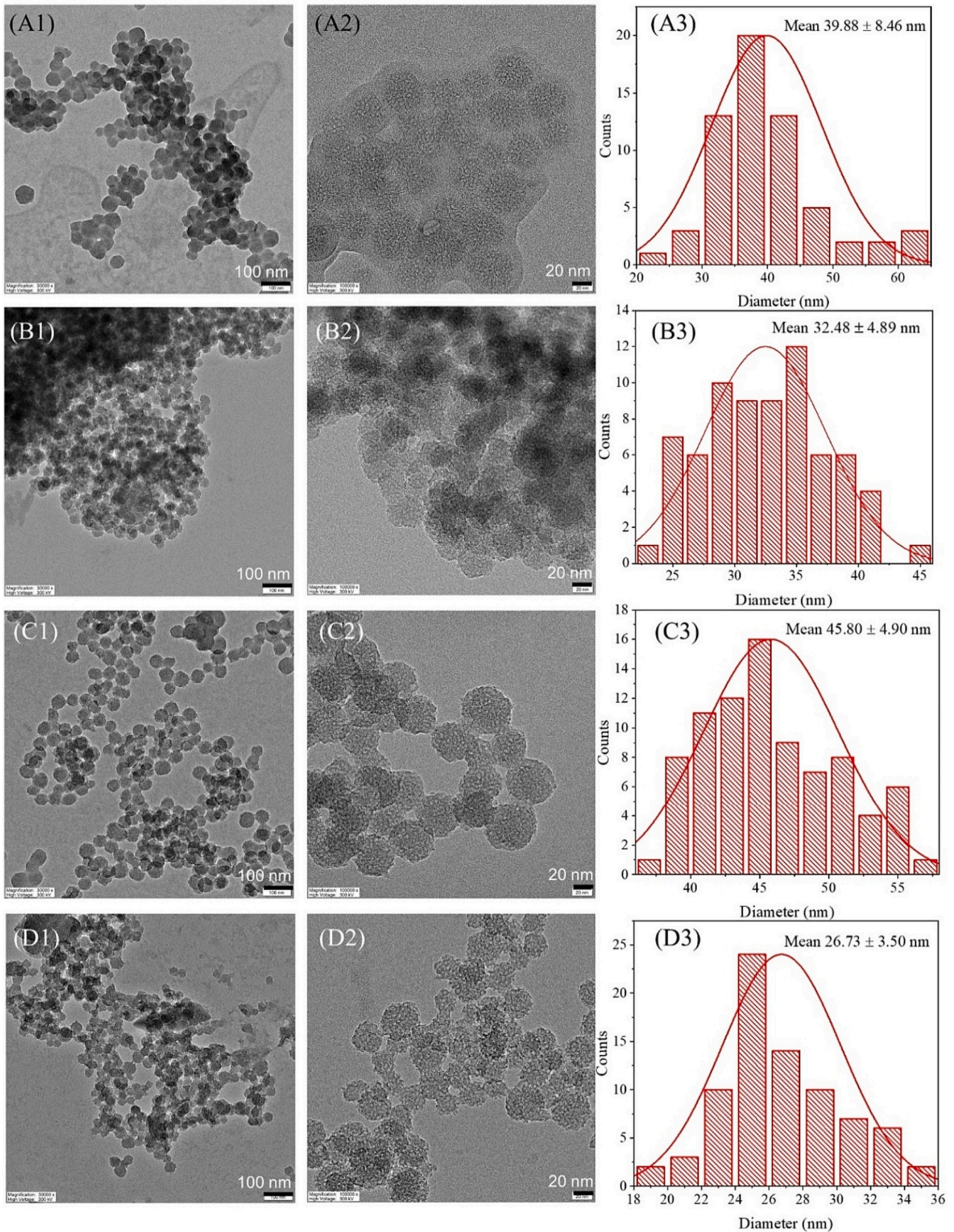
Fig. 5. FETEM imaging of different samples: (A) CDs@MSN, (B)0.20 M NS/CDs@MSN, (C)0.40 M NS/CDs@MSN and (D) MSN after reflux in the form of mesoporous silica nanoparticles (MSN) when 1) FETEM images at 10,000× or 30,000× magnification, 2) FETEM images at 100,000× magnification, and 3) average diameter and size distribution of nanoparticles.
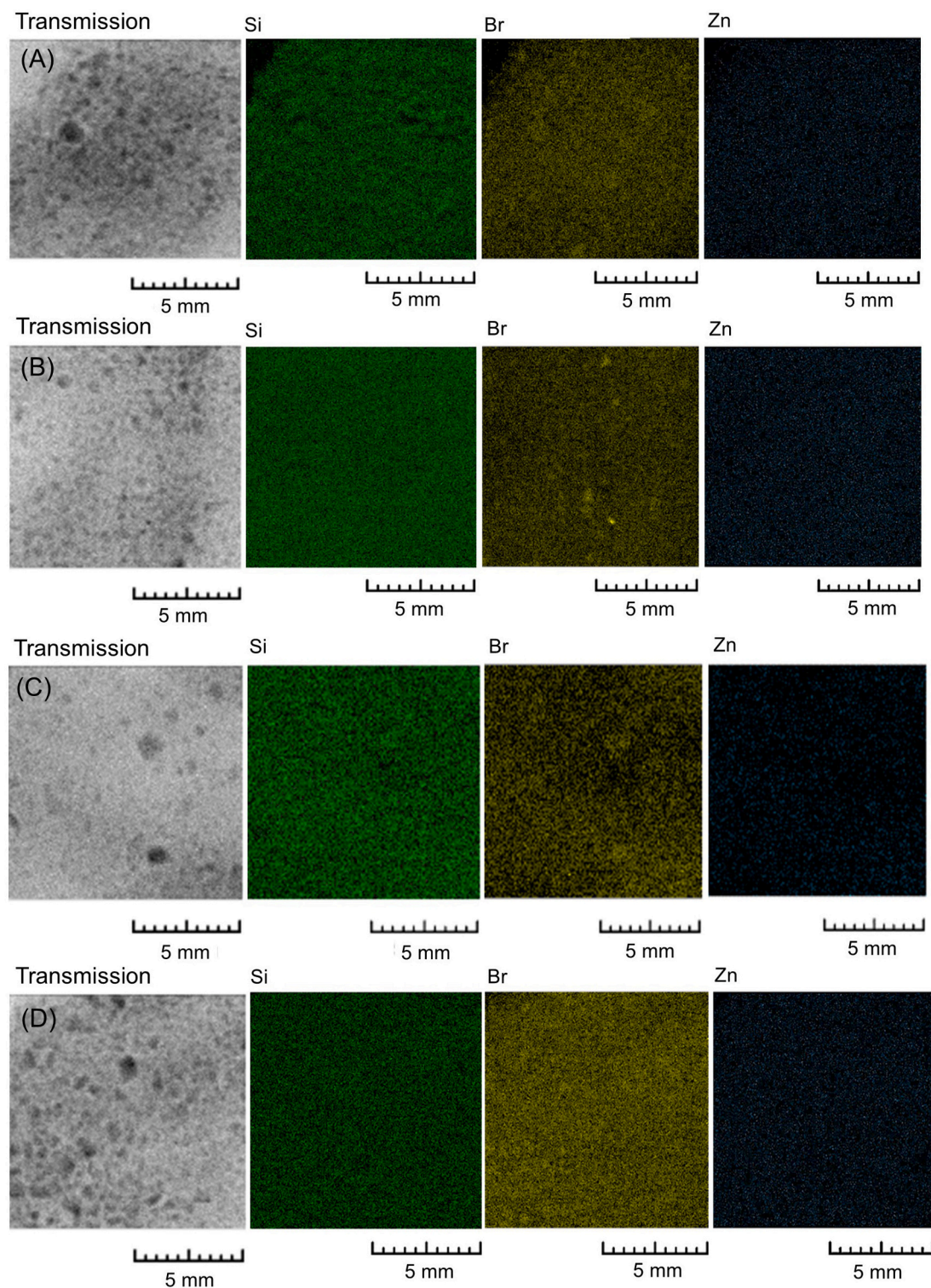
Fig. 6. XRF data analysis of different samples: (A) CDs@MSN, (B) 0.20 M NS/CDs@MSN, (C) 0.40 M NS/CDs@MSN and (D) MSN after reflux in MSN form.

information of advantages of these nanomaterials for antimicrobial drug cargo and various targeted molecule encapsulation for delivery purpose.

FESEM images demonstrated the morphology of CDs@MSN and NS/CDs@MSN synthesized as illustrated in Fig. 3. From the SEM images, the shape of MSN without and with adding carbon dots (CDs or NS/CDs) was spherical for all samples with excellent particle size uniformity. The average diameter of MSN from FESEM images was ~19.8 nm (Fig. 3(D)). Formation of nanocomposites with either CDs or NS/CDs made MSN nanoparticles' characteristics changed i.e., surface morphology and particle size. The CDs@MSN (~23.1 nm) likewise appeared spherical (Fig. 3(A)) but the particle size was larger than MSN. The average size of 0.20 M NS/CDs@MSN at ~20.5 (Fig. 3(B)) was not markedly changed compared to CDs@MSN, however the average size of 0.40 M NS/CDs@MSN (~46.4 nm) was largest among all samples as shown in Fig. 3(C). Similar trend was observed by FETEM images and size analysis (Fig. 5). More accurate size distribution was calculated using FETEM images as demonstrated in Fig. 4 and Fig. 5 for the samples before and after reflux, respectively.
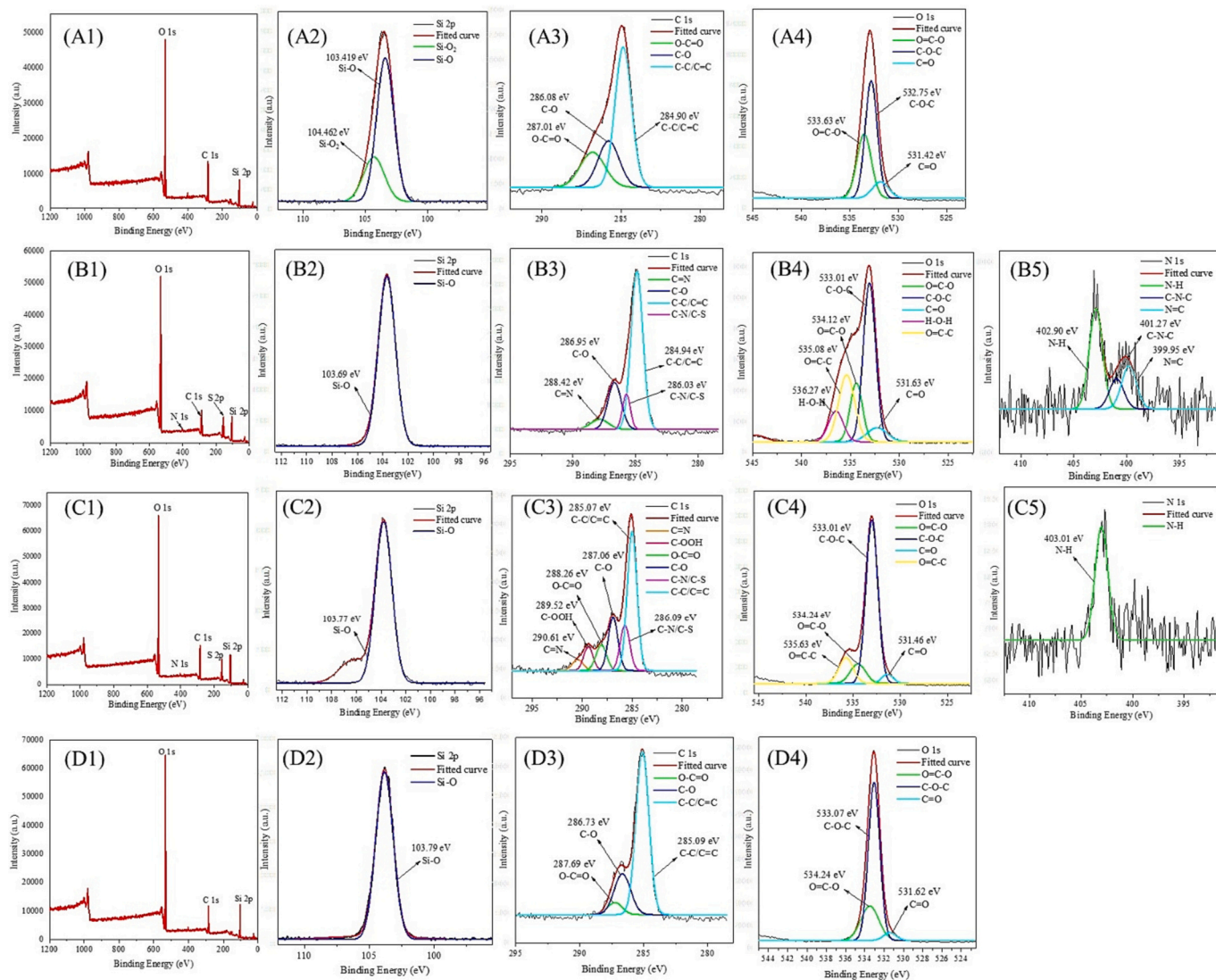
Fig. 7. High resolution XPS spectra of (A) CDs@MSN, (B) 0.20 M NS/CDs@MSN, (C) 0.40 M NS/CDs@MSN, and (D) MSN for [1] Survey, [2] O 1 s, [3] C 1 s, [4] Si 2p, and [5] N 1 s.

Morphology of CDs@SiO$_2$, and NS/CDs@SiO$_2$ before reflux characterized by FETEM imaging was demonsrtated in Fig. 4 while that of CDs@MSN, and NS/CDs@MSN after reflux was characterized as demonstrated in Fig. 5. From the result, the silicon dioxide nanoparticles after drying (before reflux with acetone) in Fig. 4 show spherical shape with unclear edge. This is seemingly refered to the greater surface roughness of silicon dioxide nanoparticle after fabrication. The average diameter of all samples was ranged from smallest to largest diameter as followed; CDs@SiO$_2$, 0.20 M NS/CDs@SiO$_2$, SiO$_2$ and 0.40 M NS/CDs@SiO$_2$ with the values of 27.33 ± 7.12 nm, 31.54 ± 3.15 nm, 35.08 ± 8.07 nm, and 41.94 ± 5.87 nm, respectively as demonstrated in Fig. 4. After reflux, the silicon dioxide nanoparticle was reduced in acetone to increase the porosity and stability yielding nanoparticles in mesoporous silica nanoparticles (MSN) form as depicted in Fig. 5. Greater average particle size was obtained for all MSN samples after reflux to eliminate CTAB surfactanct and enhance porosity compared with SiO$_2$ form before reflux. Besides, similar trend of the average diameter of MSN nanocomposite was obtained relative to SiO$_2$ before reflux as follows MSN < 0.20 M NS/CDs@MSN < CDs@MSN < 0.40 M NS/CDs@MSN of 26.73 ± 3.50 nm, 32.48 ± 4.89 nm, 39.88 ± 8.46 nm, and 45.80 ± 4.90 nm, respectively (Fig. 5). This was mainly because after reduction in acetone, the arrangement of silica particle was slightly altered and the layer of

surface edge appeared to be sharper than SiO$_2$ nanoparticles in the prior step. It was clearly seen that high content of N,S doped CDs could substantially increase the average particle size of the NS/CDs@MSN hybrid nanoparticles, therefore the greatest particle size was obtained from 0.40 M NS/CDs@MSN. In-detailed analysis of surface state of SiO$_2$ and MSN was discussed via XRF and XPS data analysis.

Figure 6 illustrates the content and distribution of silica (Si) as well as trace amount of bromine (Br) and zinc (Zn) from the precursors detected in the synthesized MSN nanocomposite from XFR analysis. The results from Fig. 6(B) and 6(C) which were 0.20 M NS/CD@MSN and 0.40 M NS/CDs@MSN demonstrated that silica was more excellently dispersed in the samples of N,S doped carbon dots compared with CDs@MSN (Fig. 6(A)) and MSN (Fig. 6(D)). This was presumably due to the binding efficiency of NS/CDs toward silica particles. From the zeta potential analysis, the surface electrostatic force of MSN was positively charged while CDs and NS/CDs from hydrothermal synthesis were found in our previous study to be highly negative charged (Saengsrichan et al., 2022a; Saengsrichan et al., 2022b). Therefore, external electrostatic force led to enhance the binding efficiency of MSN toward the surface of all CDs, and NS/CDs.

The elemental binding energy at the surface state of all samples was characterized through XPS technique as shown in Fig. 7. It was observed

Table 2

Antimicrobial activity test of CDs, NS/CDs, CDs@MSN, NS/CDs@MSN toward the growth of *Staphylococcus aureus* (ATCC 25923), *Escherichia coli* (ATCC 25922) and *Pseudomonas aeruginosa* (ATCC 27853).

Samples	Microorganisms	Antimicrobial susceptibility test		
		Diameter of inhibition zone (mm)	MICs (mg mL^{-1})	MBCs (mg mL^{-1})
CDs[a]	*P. aeruginosa*	0.00	25.00	> 50.00
	S. aureus	0.00	> 50.00	> 50.00
	E. coli	0.00	> 50.00	> 50.00
0.10 M NS/CDs[b]	*P. aeruginosa*	0.00	NA	NA
	S. aureus	0.00	NA	NA
	E. coli	0.00	NA	NA
0.20 M NS/CDs[c]	*P. aeruginosa*	0.00	12.50	> 50.00
	S. aureus	0.00	6.25	> 50.00
	E. coli	0.00	12.50	> 50.00
0.30 M NS/CDs[d]	*P. aeruginosa*	0.00	NA	NA
	S. aureus	0.00	NA	NA
	E. coli	0.00	NA	NA
0.40 M NS/CDs[d]	*P. aeruginosa*	0.00	3.125	25.00
	S. aureus	0.00	2.56	25.00
	E. coli	0.00	6.25	> 50.00
PtNPs/CDs[e]	*P. aeruginosa*	0.00	> 50.00	> 50.00
	S. aureus	0.00	12.50	> 50.00
	E. coli	0.00	12.50	> 50.00
AgNPs/CDs[f]	*P. aeruginosa*	10.0	12.50	25.00
	S. aureus	9.7	6.25	25.00
	E. coli	9.0	25.00	> 50.00
CDs@MSN	*P. aeruginosa*	NA	>250	>250
	S. aureus	NA	0.06	7.81
	E. coli	NA	31.25	125.00
0.20 M NS/CDs@MSN	*P. aeruginosa*	NA	>250	>250
	S. aureus	NA	0.03	3.91
	E. coli	NA	0.98	3.91
0.40 M NS/CDs@MSN	*P. aeruginosa*	NA	>250	>250
	S. aureus	NA	0.02	3.91
	E. coli	NA	0.06	0.24
MSN	*P. aeruginosa*	NA	>250	>250
	S. aureus	NA	0.06	3.91
	E. coli	NA	0.49	0.98

For diffusion test.
[a] CDs at 0.30 mg mL^{-1}.
[b] 0.10 M NS/CDs at 0.65 mg mL^{-1}.
[c] 0.20 M NS/CDs at 1.10 mg mL^{-1}.
[d] 0.30 M and 0.40 M NS/CDs at 1.30 mg mL^{-1}.
[e] 0.30 M NS/CDs at 2.85 mg mL^{-1}.
[f] 0.30 M NS/CDs at 3.30 mg mL^{-1}, concentration of MIC and MBC test for all samples was 50 mg mL^{-1}. MIC = minimum inhibitory concentration, and MBC = minimum bacteria concentration.

that significant sharp peak of O 1 s was found followed by C1s and Si2p for the CDs@MSN, 0.20 M NS/CDs@ MSN and 0.40 M NS/CDs@MSN samples as shown in Fig. 7(A1), 7(B1), 7(C1), respectively. In case of the control (MSN) without addition of CDs, the lower peak intensity of C1s was observed but Si2p was instead more intense (Fig. 7(D1)). The findings were in good accordance to FETEM images and XRF data since in addition to N═C and C-N-C bonds from NS/CDs synthesis, a strong binding between N and H of silica mesoporous structure was found at high amplitude in case of 0.20 M NS/CDs@MSN (Fig. 7(B5)) and particularly more intense in case of 0.40 M NS/CDs@ MSN (Fig. 7(C5)). The results agree with atomic content in the MSN nanocomposite demonstrated in Table S1.

3.2. In vitro antimicrobial and biofilm forming inhibition activities of CDs and CDs@MSN

The antimicrobial and bactericidal activities of CDs and NS/CDs as well as CDs@MSN and NS/CDs@MSN nanocomposites against *P. aeruginosa*, *S. aureus*, and *E. coli* were studied as demonstrated in Table 2. To monitor the inhibitory effect of different CDs, NS/CDs,

Table 3

Effect of nanocomposites on biofilm inhibition activity against *Staphylococcus aureus*.

Sample	Minimum biofilm inhibition concentration
CDs@MSN	25 mg mL^{-1}
0.20 M NS/CDs@MSN	0.5 mg mL^{-1}
0.40 M NS/CDs@MSN	< 0.125 mg mL^{-1}
MSN	50 mg mL^{-1}

CDs@MSN and NS/CDs@MSN concentrations, the broth microdilution checkerboard method was used to obtain MIC and MBC of individual nanoparticles. In case of diffusion test expressed as diameter of inhibition zone, only Ag nanoparticles doped CDs played a vital role on significant occurrence of the clearance zone. Analysis of CDs@MSN, NS/CDs@MSN, and MSN toward MIC and MBC (Table 2) revealed that silica nanoparticles showed significant effect on antimicrobial activity especially toward *S. aureus* and *E. coli* while less effect was found toward *P. aeruginosa*. However, the combination of NS/CDs and MSN namely 0.40 M NS/CDs@MSN and 0.20 M NS/CDs@MSN exhibited considerable inhibition of microbial growth as follows: *S. aureus* > *P. aeruginosa* > *E. coli* as demonstrated in Table 2. The strongest bacterial inhibitory effect of 0.40 M NS/CDs@MSN and 0.20 M NS/CDs@MSN was even greater than silver and platinum nanoparticles. Silver, quantum dots and several metal nanoparticles e.g., titanium dioxide, iron oxide, copper, gold nanoparticles in a correlation with their particle size, shape, surface area, and chemistry have been known to generate reactive oxygen species (ROS) from water and air at microenvironment for therapeutic application (Abdal Dayem et al., 2017). The microbial growth was suppressed regarding the damage at their molecular structure such as cell membrane at lipid layer, protein layer and DNA level (Wang et al., 2017). Additionally, it was reported that the antibacterial activity of the lipid bilayer is influenced by the fatty acid chains and their interaction with the nitrogen group (Kim et al., 2020). The presence of substantial amino/imine functional groups in N-CDs could engage in electrostatic interactions with the anionic sites of the lipid phosphate, causing an uneven distribution of surface charge on the lipid bilayer membrane. This disruption leads to the destabilization of the membrane composition, consequently increasing the permeability of the plasma membrane (Travlou et al., 2018). As a consequence, low molecular weight compounds such as potassium ions are prone to leakage (Sun et al., 2021). Apart from that, sulfur atoms in heteroatom NS/CDs@MSN generate ROS stress, which denatures proteins and lipids (Travlou et al., 2018). Indeed, there is a suggestion that sulfur metabolites can interact with cellular lipids, leading to a reduction in the overall lipid content within the cells. This interaction may result in the release of cellular components, which in turn can inhibit the viability of microorganisms (Ezati et al., 2022; Kim et al., 2020).

Since the majority of causative pathogens skin and wound infection is *S. aureus* and it additionally causes of delayed healing and infection in both acute and chronic wounds (Bessa et al., 2015; Bowler et al., 2001), the anti-biofilm activity of CDs@MSN and NS/CDs@MSN against the biofilm formation activity in *S. aureus* was investigated, as shown in Table 3. All nanoparticles prepared demonstrated anti-biofilm activity against *S. aureus*. Among all the potential nanocomposites selected for antibiofilm activity test, 0.40 M NS/CDs@MSN showed the lowest minimal biofilm inhibitory concentration (< 0.125 mg mL^{-1}), followed by 0.20 M NS/CDs@MSN (0.5 mg mL^{-1}), CD@MSN (25 mg mL^{-1}), and MSN (50 mg mL^{-1}), respectively. This suggested that these materials had antimicrobial activity and anti-biofilm activity.

From the above consequence, it was presumably that synergistic effect of NS/CDs and MSN, which were photo-responsive nanomaterial under natural light which contains wide spectrum of photon from UV to visible wavelength range, could substantially enhance the ROS generation by photocatalysis at near room temperature during microbial growth and thus led to inhibitory effect toward microbial cells as
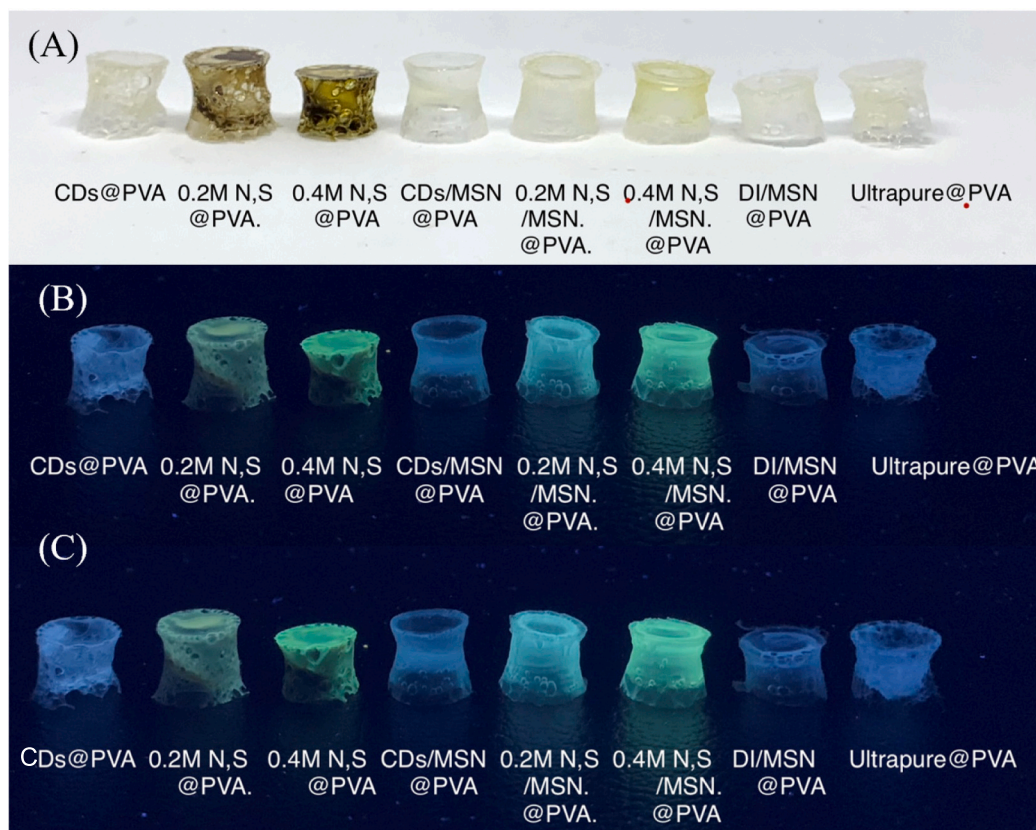
Fig. 8. Appearance of carbon dots and MSN@PVA hydrogels under (A) natural light, (B) UV light at 254 nm, and (C) UV light at 365 nm.

aforementioned.

3.3. Fabrication of CDs/MSN@PVA hydrogels, characterization and their antibiofilm and antimicrobial activities

CDs/MSN@PVA and NS/CDs/MSN@PVA hydrogels were synthesized using repeatedly freezing-thawing technique. After 15 cycles, hydrogel was perfectly formed for all samples as shown in Fig. 8. Fluorescent property of CDs/MSN@PVA, NS/CDs/MSN@PVA, and neat PVA hydrogels was investigated under natural light, and UVs irradiation at wavelength of 254 and 365 nm. In the absence of CDs, MSN and PVA hydrogel exhibited as blue emissive hydrogels while PVA hydrogel in the presence of CDs, 0.20 M NS/CDs@PVA and 0.40 M NS/CDs@PVA showed the shift of fluorescent emission from blue to light green. In other words, the red-shift phenomenon from shorter to longer wavelength of excitation occurred demonstrating the photo-responsive NS/CDs/MSN@PVA hydrogel in a wider range of light source from UV to visible spectrum (270 nm to near 400 nm) of excitation wavelength. This characteristic of NS/CDs@MSN nanocomposite could confirm the possibility of ROS generation due to day-light excitation. Beside, the finding facilitates the implementation of this nanocomposite in tunable photoluminescent cellular imaging and photonic sensing application (Liu et al., 2019a).

TGA analysis of hydrogels in Fig. 9(A) showed similar characteristic profiles of weight loss for CDs@PVA, NS/CDs@PVA, CD/MSN@PVA and NS/CDs/MSN@PVA hydrogels compared with neat PVA hydrogel at which the onset thermal degradation temperature was found at 250 °C and the final degradation temperature was at 470–480 °C. The final weight of neat PVA was 0.61 wt% while that of hybrid silica/PVA was increased to 3.0–4.8 wt%. More specifically, MSN@PVA yielded 3.50 wt % and 0.40 M NS/CDs/MSN@PVA yielded maximum residual weight of 4.82 wt% at 800 °C. When DTG profiles were considered as demonstrated in Fig. 9(B), neat PVA hydrogel exhibited three degradation

peaks at 150–160 °C, 340–350 °C and 440–450 °C while the hybrid carbon dots and silica@PVA hydrogel especially CDs@PVA, MSN@PVA and 0.40 M NS/CDs/MSN@PVA gave substantially higher degradation rate at higher temperature of 340–350 °C. The NS/CDs@PVA (i.e., 0.20 M NS/CDs@PVA and 0.40 M NS/CDs@PVA) provided highest degradation peak at 440–450 °C. The findings suggested the greater thermal stability of MSN@PVA and NS/CDs@PVA hybrid hydrogel compared with pure PVA hydrogel. Similar results were reported in previous studies when silica and alumina were hybridized with PVA matrix (Chen et al., 2010; Pingan et al., 2017).

The phase transition and crystallinity of PVA hydrogel were analyzed by DSC technique which is one of the most sensitive thermal characterization methods. As shown in Fig. 9(C), two endothermic peaks for all CDs, NS/CDs and NS/CDs@MSN hybrid PVA hydrogels were detected at 120–130 °C and 250–270 °C while only one peak at 250–270 °C was detected for pure PVA hydrogel. The prominent endothermic peak at 120–125 °C designates the melting of carbon dots in PVA matrix, and MSN in PVA matrix, while a minor hump around 250–270 °C was presumably accounted to the PVA glass transition temperature (T_g). It must be noted that although the highest endothermic peaks were fluctuated around the center of 120–125 °C, however the onset temperature of melting peaks was differed among all samples. This was mainly owing to the presence of different nanocomposites namely CDs, NS/CDs, CDs@MSN, NS/CDs@MSN and MSN. Apart from that, the melting peaks provide quantitative information of the degree of crystallinity of the polymeric hydrogels (Auriemma et al., 2008). It has been disclosed that hybrid material between inorganic filler and PVA polymeric matrix could reduce the crystallite size and decrease the crystallization, therefore the melting point (T_m) of silica@PVA material was shifted from >204 °C to lower than 150 °C. From the DSC endothermic patterns, the results suggested that 0.20 M NS/CDs@PVA and 0.40 M NS/CDs@PVA had smallest crystallite size and thus the T_m was shifted to lowest temperature (Chen et al., 2010) around 110–120 °C while
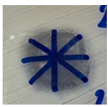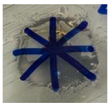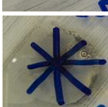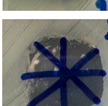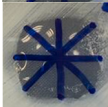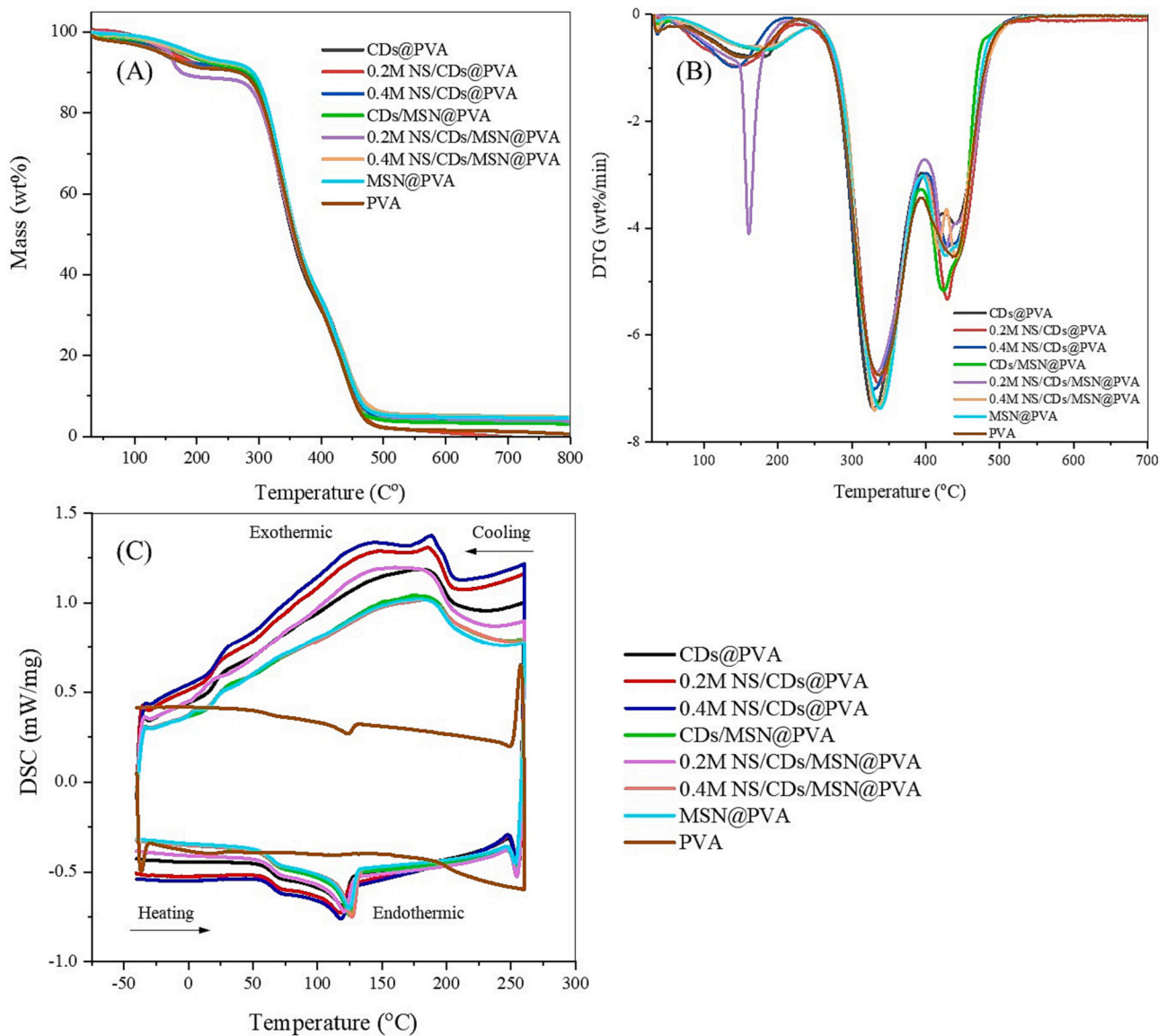
Fig. 9. (A) TGA, (B) DTG profiles, and (C) DSC patterns of CDs, NS/CDs, CDs@MSN, NS/CDs@MSN PVA hydrogels.

silica@PVA hybrids i.e., 0.40 M NS/CDs/MSN@PVA, CDs/MSN@PVA and MSN@PVA shifted the T_m to highest temperature around 125–130 °C indicating either greater crystallite size during freezing or strongest binding efficiency of carbon dots/silica@PVA hybrid material.

In case of exothermic peaks for analysis of crystallization temperature (T_c), it was observed that the exotherms upon cooling from the melt of all samples were broad, thus presenting amorphous structure with low crystallinity of all PVA hydrogel due to the freeze-thaw crosslinking technique. The greatest peak area of exothermic profile was found in 0.40 M NS/CDs@PVA and 0.20 M NS/CDs@PVA hydrogels which were significantly higher than that of all NS/CDs/MSN@PVA and neat PVA hydrogels. This apparently indicated promising efficiency of crosslinking binding of NS/CDs toward PVA structure, and consequently provided smallest crystallite size from aforementioned endotherms interpretation. Adding MSN into the PVA polymeric matrix provided smallest exothermic energy without shifting crystallization peaks of samples during cooling process. This revealed that CDs/MSN@PVA, 0.20 M NS/CDs/MSN@PVA and 0.40 M NS/CDs/MSN@PVA were easiest to form nanocomposite materials (Chen et al., 2022). The presence of MSN considerably assisted the crosslinking reaction between carbon dots and PVA matrix.

Study on diffusion test of fabricated PVA hydrogels on antibiofilm formation and antimicrobial activity was performed. As demonstrated in Table 4, 0.40 M NS/CDs/MSN@PVA hydrogel provided greatest antibiofilm activity and inhibited *S. aureus* at greatest diameter of clear zone of 23.50 ± 0.58 mm. CDs@PVA hydrogel also showed inhibitory effect on *S. aureus* growth but gave lowest inhibition at 21.00 ± 0.81 mm. For antibiofilm activity of PVA hydrogel when compared with and without MSN, it was obvious that addition of MSN achieved superior antibiofilm and antibacterial activity. From the results, the inhibition effect of PVA composite hydrogel against *S. aureus* growth was 0.40 M NS/CDs/MSN@PVA > 0.40 M NS/CDs@PVA > 0.20 M NS/CDs/MSN@PVA > 0.20 M NS/CDs@PVA > MSN@PVA > CDs@PVA, respectively. The inhibition zone and the clearness of the zone were reported in Table 4. This phenomenon was primarily because of UV-to-visible light-induced antimicrobial activity and biofilm controlling ability from photocatalytic generation of reactive oxygen species or ROS namely OH·, ROO·, O_2·-, $^1O_2$, etc. (Colilla and Vallet-Regí, 2020; Huang et al., 2023; Sakdaronnarong et al., 2020). These ROS could substantially be produced from photo-induced scission of water and air due to the electron transfer in MSN and carbon dots as mentioned in fluorescent excitation and emission characteristics of NS/CDs@MSN nanocomposites.

Table 4
Influence of different PVA hydrogels on antimicrobial and antibiofilm forming activity against *Staphylococcus aureus*.

Hydrogel Samples	Clear zone diameter (mm)	Photographs of Clear Zone	Clear zone clarity
CDs@PVA	21.00 ± 0.81		***
0.20 M NS/CDs@PVA	22.25 ± 1.26		**
0.20 M NS/CDs/MSN@PVA	22.75 ± 1.50		****
0.40 M NS/CDs@PVA	23.00 ± 0.00		***
0.40 M NS/CDs/MSN@PVA	23.50 ± 0.58		****
MSN@PVA	22.25 ± 1.71		***

Scheme 2 illustrates the photo-responsive reactivity to form ROS by CD@MSN and NS/CDs@MSN nanocomposites added in PVA hydrogels that could prevent the biofilm formation and provide the microbial inhibitory effect against *S. aureus* growth. Apart from ROS that cause cellular damage at bacterial cellular structure level due to diffusion of nanocomposites into the microbial cells (Abdal Dayem et al., 2017), it was proposed that the bactericidal activity of the conjugated NS/CDs and MSN was related to their specific surface chemistry, and their nanometer-size of particles. The electrostatic interactions between their protonated forms of amides and amines group as well as sulfonic/carboxylic and sulfate groups of N- and S- doped CDs, respectively and the cellular lipid and protein layers of the bacterial membrane have been found to cause the bactericidal function (Travlou et al., 2018). Apart from intracellular destruction of microbial by NS/CDs@MSN diffusion, surface chemistry of nanocomposites by chemical/physical modification considerably affects the microbial adhesion and thus resulting in either preventing biofilm formation or biofilm disaggregation (Lin et al., 2018).
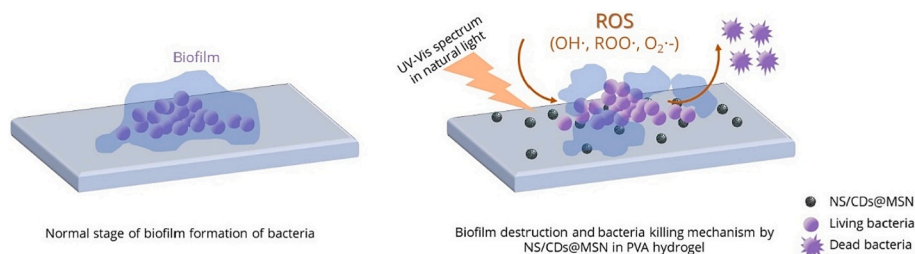
3.4. Cytotoxicity study of 0.40 M NS/CDs@PVA and 0.40 M NS/CDs/MSN@PVA hydrogels on mammalian fibroblasts (NIH/3 T3 and L-929 Cells)

Cytotoxicity study of 0.40 M NS/CDs@PVA and 0.40 M NS/CDs/MSN@PVA hydrogels on mouse fibroblast cell lines (NIH/3 T3 and L-929 Cells) obtained from the National Health Research Institute, Taiwan) was investigated as illustrated in Fig. 10. From the results, no significant effect of the hydrogel extracts from both 0.40 M NS/CDs@PVA and 0.40 M NS/CDs-MSN@PVA hydrogels toward NIH/3 T3 cell viability (Fig. 10(A) and 10(B), respectively). Cell viability was as high as 95% to 100% from all concentrations of gel extracts between 20 and 100% which corresponded to 20 mg gel mL^{-1} extract solution. Likewise, the result in Fig. 10(C) demonstrated that 0.40 M NS/CDs@PVA did not affect the L-929 cell viability (99–100 cell viability) even at highest concentration of extracts at 100%. However, synergistic effect of MSN composited on NS/CDs in PVA hydrogels showed slightly reduction of L-929 cells viability which was reduced to 81.6% cell viability at 100% of 0.40 M NS/CDs-MSN@PVA hydrogel extract as illustrated in Fig. 10(D).

In general, living mammalian cells employ different mechanisms to internalize extracellular materials. Various endocytosis processes were classified and clathrin-mediated endocytosis (Ferreira and Boucrot, 2018) was the most suitable model to describe the pathway of uptaken cargo molecules smaller than 200 nm (Rejman et al., 2004). Recently, it has been reported on a slower CDs penetration rate into NIH/3 T3 cells compared with L-929 cells from the real-time monitoring of CDs uptake across the plasma cell membrane of both types of fibroblast cells, and the endocytic pathway was identified (Havrdová et al., 2021). High concentration of CDs could cause disruption of L-929 cells' nuclear membrane and thus penetrated to the nucleus and evoked cellular death. However, positively charged CDs was reported not suitable for L-929 cellular labelling. However, the different circumstance was found in NIH/3 T3 cell line in which the obvious slower uptake rate of CDs and more prudent was detected. NIH/3 T3 cell line showed insignificant changes in cell viability and DNA damage, nonetheless the cell cycle profile was observed to be altered.

In the present study, the effect of nitrogen- and sulfur-doped CDs (NS/CDs) and MSN composites provided both 1) bactericidal activity to inactivate the bacterial growth (Table 2) through disrupting cell membrane and killing bacteria similar to other nanomaterials which might cause cytotoxicity (Hu et al., 2017), and 2) ability to prevent biofilm formation of bacteria i.e., *S. aureus* (Table 3) which was conceivably through sulfur metabolism (Wood, 2009), cysteine metabolism (Lee et al., 2007) or cell signaling (Wood, 2009), as observed for other nontoxic biofilm inhibitors. Regarding low toxicity and high biocompatibility of NS/CDs@MSN (carbon dots/mesoporous silica hybrid nanomaterial) as well as their tunable photonic property and functionality, the present work newly reported on their performance as a bioimaging and biosensor to selectively detect some biomolecules *in vitro* and specific compounds (Ornelas-Hernández et al., 2022) as well as drug delivery for nanotheranostic application (Kajani et al., 2023). Consequently, 0.40 M NS/CDs@MSN in the present study is one of
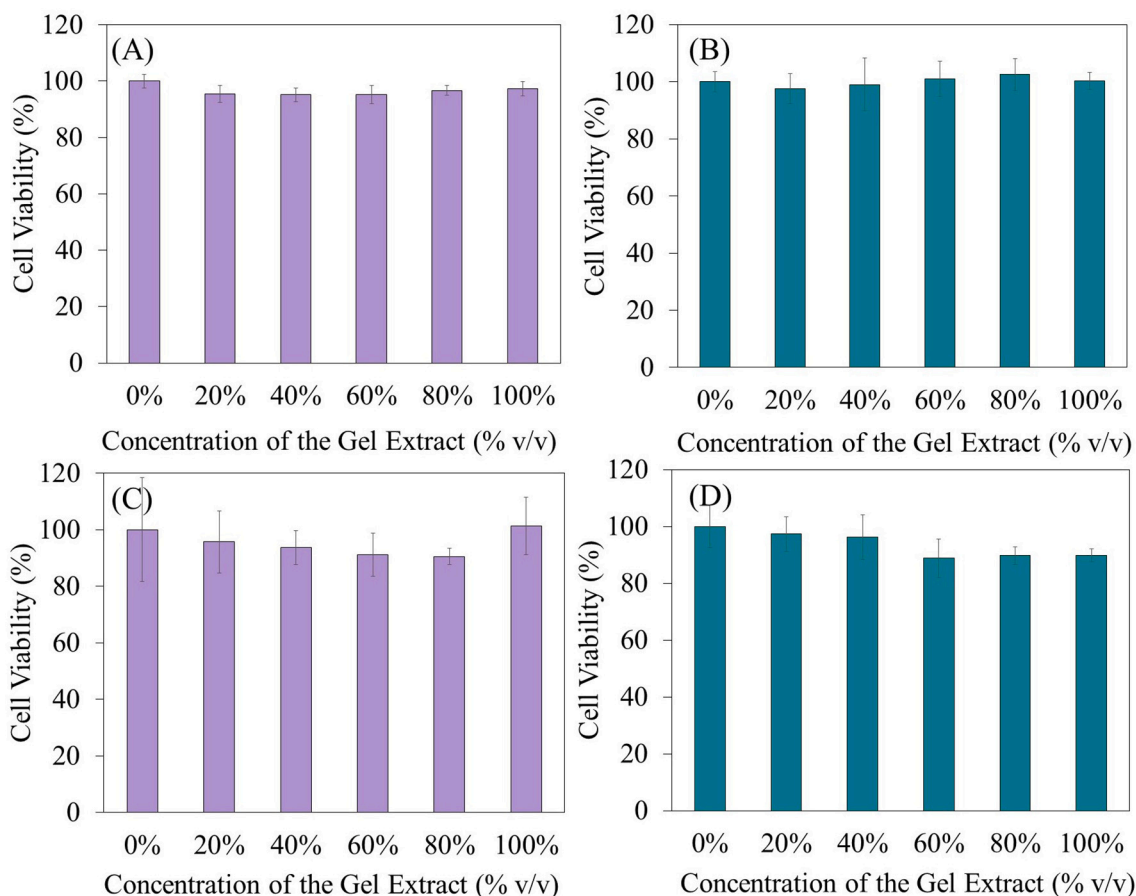

Scheme 2. The schematic illustration of antibiofilm activity of NS/CDs@MSN in PVA hydrogel from repeatedly freezing-thawing technique.

Fig. 10. Cell viability using MTT assay (A) 0.40 M NS/CDs@PVA hydrogel extract, and (B) 0.40 M NS/CDs-MSN@PVA hydrogel extract toward NIH/3 T3 cells, and (C) 0.40 M NS/CDs@PVA hydrogel extract, and (D) 0.40 M NS/CDs-MSN@PVA hydrogel extract toward L-929 cells.

promising hybrid nanoparticles providing anti-inflammatory effect, antimicrobial activity and biofilm controlling efficiency for wound healing and wound dressing applications.

4. Conclusion

In order to control the bacterial biofilm formation which led to enhance antimicrobial activity, mesoporous silica nanoparticles (MSN) were synthesized and used as a hollow template for carbon dots (CDs) immobilization. The finding provided detailed information on photo-responsive electron transport between MSN and CDs or nitrogen- and sulfur-doped carbon dots (NS/CDs) locations through their fluorescence emissive characteristics at different light spectral wavelength between 270 nm to 400 nm. Reactive oxygen species (ROS) generated from natural light-induced phenomenon were believed to play an important role in destruction of bacterial biofilm and thus led to an increased antimicrobial activity. From the antimicrobial activity test, it was found that MSN itself showed significant antimicrobial activity greater than silver nanoparticles for over 4 times against all bateria tested, and especially 100 times against *Staphylococcus aureus*. The combination of NS/CDs and MSN nanocomposite substantially amplified both pre-venting biofilm formation due to their surface chemical interaction, and antimicrobial activity due to intercellular bacterial destruction through generated ROS. The results indicated a promising potential of cost-effective nitrogen- and sulfur-doped carbon dots and mesoporous silica nanoparticles nanocomposite for biomedical application. This nanocomposite was straightforwardly synthesized and demonstrated effective biofilm control and antimicrobial properties, making it a valuable candidate for application in chronic wound healing.

CRediT authorship contribution statement

Pisut Pongchaikul: Conceptualization, Methodology, Formal anal-ysis, Investigation, Writing – original draft. **Tasnim Hajidariyor:** Formal analysis, Investigation, Data curation, Writing – original draft. **Navarat Khetlai:** Formal analysis, Investigation, Formal analysis, Data curation, Writing – original draft. **Yu-Sheng Yu:** Methodology, Formal analysis, Investigation, Formal analysis, Data curation, Writing – orig-inal draft. **Pariyapat Arjfuk:** Conceptualization, Validation, Visualiza-tion, Supervision. **Pongtanawat Khemthong:** Conceptualization, Validation, Visualization, Supervision. **Wanwitoo Wanmolee:** Conceptualization, Validation, Visualization, Supervision. **Pattaraporn Posoknistakul:** Conceptualization, Validation, Visualization, Supervi-sion. **Navadol Laosiripojana:** Conceptualization, Validation, Visuali-zation, Supervision. **Kevin C.-W. Wu:** Conceptualization, Methodology, Supervision, Validation, Writing – original draft, Writing – review & editing. **Chularat Sakdaronnarong:** Conceptualization, Methodology, Formal analysis, Data curation, Supervision, Validation, Writing – original draft, Writing – review & editing, Funding acquisition, Project administration.

Declaration of Competing Interest

The authors declare that they have no known competing financial interests or personal relationships that could have appeared to influence the work reported in this paper.

Data availability

Data will be made available on request.

Appendix A. Supplementary data

Supplementary data to this article can be found online at https://doi.org/10.1016/j.ijpx.2023.100209.

References

Abbasi, M., Gholizadeh, R., Kasaee, S.R., Vaez, A., Chelliapan, S., Fadhil Al-Qaim, F., Deyab, I.F., Shafiee, M., Zareshahrabadi, Z., Amani, A.M., Mosleh-Shirazi, S., Kamyab, H., 2023. An intriguing approach toward antibacterial activity of green synthesized Rutin-templated mesoporous silica nanoparticles decorated with nanosilver. Sci. Rep. 13, 5987.

Abdal Dayem, A., Hossain, M.K., Lee, S.B., Kim, K., Saha, S.K., Yang, G.M., Choi, H.Y., Cho, S.G., 2017. The Role of Reactive Oxygen Species (ROS) in the biological activities of metallic nanoparticles. Int. J. Mol. Sci. 18.

Auriemma, F., De Rosa, C., Ricciardi, R., Lo Celso, F., Triolo, R., Pipich, V., 2008. Time-resolving analysis of cryotropic gelation of water/poly(vinyl alcohol) solutions via small-angle neutron scattering. J. Phys. Chem. B 112, 816–823.

Baig, M.M., Zulfiqar, S., Yousuf, M.A., Shakir, I., Aboud, M.F.A., Warsi, M.F., 2021. DyxMnFe2-xO4 nanoparticles decorated over mesoporous silica for environmental remediation applications. J. Hazard. Mater. 402, 123526.

Bernardos, A., Piacenza, E., Sancenón, F., Hamidi, M., Maleki, A., Turner, R.J., Martínez-Máñez, R., 2019. Mesoporous silica-based materials with bactericidal properties. Small 15, 1900669.

Bessa, L.J., Fazii, P., Di Giulio, M., Cellini, L., 2015. Bacterial isolates from infected wounds and their antibiotic susceptibility pattern: some remarks about wound infection. Int. Wound J. 12, 47–52.

Bjarnsholt, T., 2013. The role of bacterial biofilms in chronic infections. APMIS Suppl. 1–51.

Bowler, P.G., Duerden, B.I., Armstrong, D.G., 2001. Wound microbiology and associated approaches to wound management. Clin. Microbiol. Rev. 14, 244–269.

Bulatović, M.Z., Maksimović-Ivanić, D., Bensing, C., Gómez-Ruiz, S., Steinborn, D., Schmidt, H., Mojić, M., Korać, A., Golić, I., Pérez-Quintanilla, D., Momčilović, M., Mijatović, S., Kaluđerović, G.N., 2014. Organotin(IV)-loaded mesoporous silica as a biocompatible strategy in cancer treatment. Angew. Chem. Int. Ed. 53, 5982–5987.

Cassat, J.E., Lee, C.Y., Smeltzer, M.S., 2007. Investigation of biofilm formation in clinical isolates of *Staphylococcus aureus*. Methods Mol. Biol. 391, 127–144.

Castillo, R.R., Vallet-Regí, M., 2021. Recent advances toward the use of mesoporous silica nanoparticles for the treatment of bacterial infections. Int. J. Nanomedicine 16, 4409–4430.

Chen, H., Zhen, Z., Tang, W., Todd, T., Chuang, Y.-J., Wang, L., Pan, Z., Xie, J., 2013. Label-free luminescent mesoporous silica nanoparticles for imaging and drug delivery. Theranostics 3, 650–657.

Chen, L., Zheng, K., Tian, X., Hu, K., Wang, R., Liu, C., Li, Y., Cui, P., 2010. Double glass transitions and interfacial immobilized layer in in-situ-synthesized poly(vinyl alcohol)/silica nanocomposites. Macromolecules 43, 1076–1082.

Chen, Y., Li, J., Lu, J., Ding, M., Chen, Y., 2022. Synthesis and properties of Poly(vinyl alcohol) hydrogels with high strength and toughness. Polym. Test. 108, 107516.

Colilla, M., Vallet-Regí, M., 2020. Targeted stimuli-responsive mesoporous silica nanoparticles for bacterial infection treatment. Int. J. Mol. Sci. 21, 8605.

Dabke, G., Sheridan, E., 2011. Antimicrobial resistance: the threat to public health. Perspect. Public Health 131, 260.

Deng, Y., Qi, D., Deng, C., Zhang, X., Zhao, D., 2008. Superparamagnetic high-magnetization microspheres with an Fe3O4@SiO2 core and perpendicularly aligned mesoporous SiO2 shell for removal of microcystins. J. Am. Chem. Soc. 130, 28–29.

Díaz-García, D., Ardiles, P.R., Prashar, S., Rodríguez-Diéguez, A., Páez, P.L., Gómez-Ruiz, S., 2019. Preparation and study of the antibacterial applications and oxidative stress induction of copper maleamate-functionalized mesoporous silica nanoparticles. Pharmaceutics 11, 30.

Díaz-García, D., Ardiles, P.R., Díaz-Sánchez, M., Mena-Palomo, I., del Hierro, I., Prashar, S., Rodríguez-Diéguez, A., Páez, P.L., Gómez-Ruiz, S., 2020. Copper-functionalized nanostructured silica-based systems: Study of the antimicrobial applications and ROS generation against gram positive and gram negative bacteria. J. Inorg. Biochem. 203, 110912.

Ding, C., Deng, Z., Chen, J., Jin, Y., 2020. One-step microwave synthesis of N,S co-doped carbon dots from 1,6-hexanediamine dihydrochloride for cell imaging and ion detection. Colloids Surf. B: Biointerfaces 189, 110838.

Dong, X., Liang, W., Meziani, M.J., Sun, Y.P., Yang, L., 2020. Carbon dots as potent antimicrobial agents. Theranostics 10, 671–686.

Ehtesabi, H., Roshani, S., Bagheri, Z., Yaghoubi-Avini, M., 2019. Carbon dots—Sodium alginate hydrogel: a novel tetracycline fluorescent sensor and adsorber. J. Environ. Chem. Eng. 7, 103419.

Ezati, P., Rhim, J.-W., Molaei, R., Priyadarshi, R., Roy, S., Min, S., Kim, Y.H., Lee, S.-G., Han, S., 2022. Preparation and characterization of B, S, and N-doped glucose carbon dots: antibacterial, antifungal, and antioxidant activity. Sustain. Mater. Technol. 32, e00397.

Ferreira, A.P.A., Boucrot, E., 2018. Mechanisms of carrier formation during clathrin-independent endocytosis. Trends Cell Biol. 28, 188–200.

Ferri, M., Ranucci, E., Romagnoli, P., Giaccone, V., 2017. Antimicrobial resistance: a global emerging threat to public health systems. Crit. Rev. Food Sci. Nutr. 57, 2857–2876.

Guerritore, M., Olivieri, F., Avolio, R., Castaldo, R., Cocca, M., Errico, M.E., Lavorgna, M., Silvestri, B., Ambrogi, V., Gentile, G., 2022. Hierarchical micro-to-macroporous silica nanoparticles obtained by their grafting with hyper-crosslinked resin. Microporous Mesoporous Mater. 335, 111864.

Gupta, S., Pramanik, A.K., Kailath, A., Mishra, T., Guha, A., Nayar, S., Sinha, A., 2009. Composition dependent structural modulations in transparent poly(vinyl alcohol) hydrogels. Colloids Surf. B: Biointerfaces 74, 186–190.

Hajidariyor, T., Nuntawad, N., Somsaen, P., Prukdamrongchai, R., Cherdchoo, H., Posoknistakul, P., Khemthong, P., Wanmolee, W., Arjfuk, P., Pongchaikul, P., Laosiripojana, N., Wu, K.C.W., Sakdaronnarong, C., 2023. Cryo-induced cellulose-based nanogel from *Elaeis guineensis* for antibiotic delivery platform. Int. J. Mol. Sci. 24.

Hao, W., Shen, Y., Liu, D., Shang, Y., Zhang, J., Xu, S., Liu, H., 2017. Dual-pH-sensitivity and tumour targeting core–shell particles for intracellular drug delivery. RSC Adv. 7, 851–860.

Havrdová, M., Urbančič, I., Bartoň Tománková, K., Malina, L., Štrancar, J., Bourlinos, A. B., 2021. Self-targeting of carbon dots into the cell nucleus: diverse mechanisms of toxicity in NIH/3T3 and L929 cells. Int. J. Mol. Sci. 22, 5608.

del Hierro, I., Pérez, Y., Cruz, P., Juárez, R., 2017. Pt and Ti complexes immobilized onto mesoporous silica microspheres and their interaction with molecules of biological interest. Eur. J. Inorg. Chem. 2017, 3030–3039.

Hu, D., Li, H., Wang, B., Ye, Z., Lei, W., Jia, F., Jin, Q., Ren, K.-F., Ji, J., 2017. Surface-adaptive gold nanoparticles with effective adherence and enhanced photothermal ablation of methicillin-resistant *Staphylococcus aureus* biofilm. ACS Nano 11, 9330–9339.

Hu, M., Gu, X., Hu, Y., Deng, Y., Wang, C., 2016. PVA/Carbon Dot Nanocomposite Hydrogels for simple Introduction of Ag Nanoparticles with Enhanced Antibacterial activity. Macromol. Mater. Eng. 301, 1352–1362.

Huang, D., Wang, Y., Xiao, J., Wang, Y., Zhu, X., Xu, B., Wang, M., 2023. Scavenging of reactive oxygen species effectively reduces *Pseudomonas aeruginosa* biofilms through disrupting policing. Environ. Res. 220, 115182.

Kajani, A.A., Rafiee, L., Javanmard, S.H., Dana, N., Jandaghian, S., 2023. Carbon dot incorporated mesoporous silica nanoparticles for targeted cancer therapy and fluorescence imaging. RSC Adv. 13, 9491–9500.

Kim, Y.H., Kim, G.H., Yoon, K.S., Shankar, S., Rhim, J.-W., 2020. Comparative antibacterial and antifungal activities of sulfur nanoparticles capped with chitosan. Microb. Pathog. 144, 104178.

King, P., McMillan, P., Moore, G., Ramsey, M., Swayze, G., 2004. Infrared spectroscopy of silicate glasses with application to natural systems. Infrar. Spectrosc. Geochem. Explor. Geochem. Remote Sens. 33, 93–133.

Lee, J., Bansal, T., Jayaraman, A., Bentley, W.E., Wood, T.K., 2007. Enterohemorrhagic *Escherichia coli* biofilms are Inhibited by 7-hydroxyindole and stimulated by Isatin. Appl. Environ. Microbiol. 73, 4100–4109.

Li, P., Sun, L., Xue, S., Qu, D., An, L., Wang, X., Sun, Z., 2022. Recent advances of carbon dots as new antimicrobial agents. SmartMat 3, 226–248.

Li, Q., Shen, X., Xing, D., 2023. Carbon quantum dots as ROS-generator and -scavenger: a comprehensive review. Dyes Pigments 208, 110784.

Lin, F., Li, C., Chen, Z., 2018. Bacteria-derived carbon dots inhibit biofilm formation of escherichia coli without affecting cell growth. Front. Microbiol. 9.

Liu, H., Zhang, Y., Huang, C., 2019a. Development of nitrogen and sulfur-doped carbon dots for cellular imaging. J. Pharma. Anal. 9, 127–132.

Liu, M., Huang, L., Xu, X., Wei, X., Yang, X., Li, X., Wang, B., Xu, Y., Li, L., Yang, Z., 2022. Copper doped carbon dots for addressing bacterial biofilm formation, wound infection, and tooth staining. ACS Nano 16, 9479–9497.

Liu, Y., Liu, X., Xiao, Y., Chen, F., Xiao, F., 2017. A multifunctional nanoplatform based on mesoporous silica nanoparticles for imaging-guided chemo/photodynamic synergetic therapy. RSC Adv. 7, 31133–31141.

Liu, Y., Jiang, L., Li, B., Fan, X., Wang, W., Liu, P., Xu, S., Luo, X., 2019b. Nitrogen doped carbon dots: mechanism investigation and their application for label free CA125 analysis. J. Mater. Chem. B 7, 3053–3058.

Manzano, M., Vallet-Regí, M., 2018. Mesoporous silica nanoparticles in nanomedicine applications. J. Mater. Sci. Mater. Med. 29, 65.

Martínez-Carmona, M., Gun'ko, Y.K., Vallet-Regí, M., 2018. Mesoporous silica materials as drug delivery: "the Nightmare" of bacterial infection. Pharmaceutics 10.

Merlino, J., 2017. Antimicrobial resistance a threat to public health. Microbiol. Austral. 38, 165–167.

Mishra, S., Gupta, A., Upadhye, V., Singh, S.C., Sinha, R.P., Häder, D.-P., 2023. Therapeutic strategies against biofilm infections. Life 13, 172.

Nayak, S., Prasad, S.R., Mandal, D., Das, P., 2020. Carbon dot cross-linked polyvinylpyrrolidone hybrid hydrogel for simultaneous dye adsorption, photodegradation and bacterial elimination from waste water. J. Hazard. Mater. 392, 122287.

Ornelas-Hernández, L.F., Garduno-Robles, A., Zepeda-Moreno, A., 2022. A brief review of carbon Dots–Silica nanoparticles synthesis and their potential use as biosensing and theragnostic applications. Nanoscale Res. Lett. 17, 56.

Pingan, H., Mengjun, J., Yanyan, Z., Ling, H., 2017. A silica/PVA adhesive hybrid material with high transparency, thermostability and mechanical strength. RSC Adv. 7, 2450–2459.

Rejman, J., Oberle, V., Zuhorn, I.S., Hoekstra, D., 2004. Size-dependent internalization of particles via the pathways of clathrin- and caveolae-mediated endocytosis. Biochem. J. 377, 159–169.

Sadek, O., Reda, S., Al-Bilali, R., 2013. Preparation and characterization of silica and clay-silica core-shell nanoparticles using sol-gel method. Adv. Nanopartic. 2, 165–175.

Saengsrichan, A., Khemthong, P., Wanmolee, W., Youngjan, S., Phanthasri, J., Arjfuk, P., Pongchaikul, P., Ratchahat, S., Posoknistakul, P., Laosiripojana, N., Wu, K.C.W., Sakdaronnarong, C., 2022a. Platinum/carbon dots nanocomposites from palm bunch hydrothermal synthesis as highly efficient peroxidase mimics for ultra-low H2O2 sensing platform through dual mode of colorimetric and fluorescent detection. Anal. Chim. Acta 1230, 340368.

Saengsrichan, A., Saikate, C., Silasana, P., Khemthong, P., Wanmolee, W., Phanthasri, J., Youngjan, S., Posoknistakul, P., Ratchahat, S., Laosiripojana, N., Wu, K.C.-W., Sakdaronnarong, C., 2022b. The Role of N and S Doping on Photoluminescent Characteristics of Carbon Dots from Palm Bunches for Fluorimetric Sensing of Fe3+ Ion. Int. J. Mol. Sci. 23, 5001.

Sahiner, N., Suner, S.S., Sahiner, M., Silan, C., 2019. Nitrogen and sulfur doped carbon dots from amino acids for potential biomedical applications. J. Fluoresc. 29, 1191–1200.

Sakdaronnarong, C., Sangjan, A., Boonsith, S., Kim, D.C., Shin, H.S., 2020. Recent developments in synthesis and photocatalytic applications of carbon dots. Catalysts 10, 320.

Sangjan, A., Boonsith, S., Sansanaphongpricha, K., Thinbanmai, T., Ratchahat, S., Laosiripojana, N., Wu, K.C.W., Shin, H.S., Sakdaronnarong, C., 2022. Facile preparation of aqueous-soluble fluorescent polyethylene glycol functionalized carbon dots from palm waste by one-pot hydrothermal carbonization for colon cancer nanotheranostics. Sci. Rep. 12.

Selvarajan, V., Obuobi, S., Ee, P.L.R., 2020. Silica nanoparticles—a versatile tool for the treatment of bacterial infections. Front. Chem. 8.

Şen Karaman, D., Manner, S., Rosenholm, J.M., 2018. Mesoporous silica nanoparticles as diagnostic and therapeutic tools: how can they combat bacterial infection? Ther. Deliv. 9, 241–244.

Sheng, Y., Peng, Y., Zhang, S., Guo, Y., Ma, L., Wang, Q., Zhang, H., 2022. Study on thermal stability of gel foam Co-stabilized by hydrophilic silica nanoparticles and surfactants. Gels 8.

Shi, L., Wu, Y., Yang, C., Ma, Y., Zhang, Q.-Z., Huang, W., Zhu, X.-Y., Yan, Y.-J., Wang, J.-X., Zhu, T., Qu, D., Zheng, C.-Q., Zhao, K.-Q., 2019. Effect of nicotine on *Staphylococcus aureus* biofilm formation and virulence factors. Sci. Rep. 9, 20243.

Song, T., Zhao, Y., Wang, T., Li, J., Jiang, Z., Yang, P., 2020. Carbon dots doped with N and S towards controlling emitting. J. Fluoresc. 30, 81–89.

Sun, B., Wu, F., Zhang, Q., Chu, X., Wang, Z., Huang, X., Li, J., Yao, C., Zhou, N., Shen, J., 2021. Insight into the effect of particle size distribution differences on the antibacterial activity of carbon dots. J. Colloid Interface Sci. 584, 505–519.

Sun, D., Ban, R., Zhang, P.-H., Wu, G.-H., Zhang, J.-R., Zhu, J.-J., 2013. Hair fiber as a precursor for synthesizing of sulfur- and nitrogen-co-doped carbon dots with tunable luminescence properties. Carbon 64, 424–434.

Supa-Amornkul, S., Mongkolsuk, P., Summpunn, P., Chaiyakunvat, P., Navaratdusit, W., Jiarpinitnun, C., Chaturongakul, S., 2019. alternative sigma factor B in bovine mastitis-causing *Staphylococcus aureus*: characterization of its role in biofilm formation, resistance to hydrogen peroxide stress, regulon members. Front. Microbiol. 10, 2493.

Travlou, N.A., Giannakoudakis, D.A., Algarra, M., Labella, A.M., Rodríguez-Castellón, E., Bandosz, T.J., 2018. S- and N-doped carbon quantum dots: surface chemistry dependent antibacterial activity. Carbon 135, 104–111.

Ugalde-Arbizu, M., Aguilera-Correa, J.J., San Sebastian, E., Páez, P.L., Nogales, E., Esteban, J., Gómez-Ruiz, S., 2023. Antibacterial properties of mesoporous silica nanoparticles modified with fluoroquinolones and copper or silver species. Pharmaceuticals 16, 961.

Wang, H., Song, Z., Gu, J., Li, S., Wu, Y., Han, H., 2019a. Nitrogen-doped carbon quantum dots for preventing biofilm formation and eradicating drug-resistant bacteria infection. ACS Biomater. Sci. Eng. 5, 4739–4749.

Wang, L., He, H., Zhang, C., Sun, L., Liu, S., Yue, R., 2014. Excellent antimicrobial properties of silver-loaded mesoporous silica SBA-15. J. Appl. Microbiol. 116, 1106–1118.

Wang, L., Zhang, H., Zhou, X., Liu, Y., Lei, B., 2016. Preparation, characterization and oxygen sensing properties of luminescent carbon dots assembled mesoporous silica microspheres. J. Colloid Interface Sci. 478, 256–262.

Wang, L., Hu, C., Shao, L., 2017. The antimicrobial activity of nanoparticles: present situation and prospects for the future. Int. J. Nanomedicine 12, 1227–1249.

Wang, M., Ren, X., Zhu, L., Xia, Y., Qiu, J., 2019b. Preparation of mesoporous silica/carbon quantum dots composite and its application in selective and sensitive Hg2+ detection. Microporous Mesoporous Mater. 284, 378–384.

Wani, W.A., Prashar, S., Shreaz, S., Gómez-Ruiz, S., 2016. Nanostructured materials functionalized with metal complexes: in search of alternatives for administering anticancer metallodrugs. Coord. Chem. Rev. 312, 67–98.

Wood, T.K., 2009. Insights on Escherichia coli biofilm formation and inhibition from whole-transcriptome profiling. Environ. Microbiol. 11, 1–15.

Wu, X., Abbas, K., Yang, Y., Li, Z., Tedesco, A.C., Bi, H., 2022. Photodynamic Anti-Bacteria by Carbon Dots and their Nano-Composites. Pharmaceuticals 15, 487.

Yusuf, M.O., 2023. Bond Characterization in Cementitious material binders using fourier-transform infrared spectroscopy. Appl. Sci. 13, 3353.

Zhang, J., Lu, X., Tang, D., Wu, S., Hou, X., Liu, J., Wu, P., 2018. Phosphorescent carbon dots for highly efficient oxygen photosensitization and as photo-oxidative nanozymes. ACS Appl. Mater. Interfaces 10, 40808–40814.

Zhao, Q., Wang, S., Yang, Y., Li, X., Di, D., Zhang, C., Jiang, T., Wang, S., 2017. Hyaluronic acid and carbon dots-gated hollow mesoporous silica for redox and enzyme-triggered targeted drug delivery and bioimaging. Mater. Sci. Eng. C 78, 475–484.

Zhao, W., Ji, W., Zhang, Y., Du, L., Wang, S., 2016. A competitive fluorescence quenching-based immunoassay for bisphenol a employing functionalized silica nanoparticles and nanogold. RSC Adv. 6, 38950–38956.

Zhao, W.-B., Liu, K.-K., Wang, Y., Li, F.-K., Guo, R., Song, S.-Y., Shan, C.-X., 2023. Antibacterial carbon dots: mechanisms, design, and applications. Adv. Healthcare Mater. 2300324 n/a.